Icarus xxx (2010) xxx–xxx

Contents lists available at ScienceDirect

Icarus

journal homepage: www.elsevier.com/locate/icarus

Mercury's magnetospheric magnetic field after the first two MESSENGER flybys

Igor I. Alexeev [a,*], Elena S. Belenkaya [a], James A. Slavin [b], Haje Korth [c], Brian J. Anderson [c], Daniel N. Baker [d], Scott A. Boardsen [b], Catherine L. Johnson [e], Michael E. Purucker [b], Menelaos Sarantos [b], Sean C. Solomon [f]

[a] Scobeltsyn Institute of Nuclear Physics, Lomonosov Moscow State University, Leninskie Gory, 119992 Moscow, Russia
[b] Heliophysics Science Division, NASA Goddard Space Flight Center, Greenbelt, MD 20771, USA
[c] The Johns Hopkins University Applied Physics Laboratory, Laurel, MD 20723, USA
[d] Laboratory for Atmospheric and Space Physics, University of Colorado, Boulder, CO 80309-7814, USA
[e] Department of Earth and Ocean Sciences, University of British Columbia, 6339 Stores Road, Vancouver, BC, Canada V6T 1Z4
[f] Department of Terrestrial Magnetism, Carnegie Institution of Washington, Washington, DC 20015, USA

ARTICLE INFO

Article history:
Received 13 October 2009
Revised 15 January 2010
Accepted 25 January 2010
Available online xxxx

Keywords:
Mercury
Magnetospheres
Magnetic fields

ABSTRACT

The "paraboloid" model of Mercury's magnetospheric magnetic field is used to determine the best-fit magnetospheric current system and internal dipole parameters from magnetic field measurements taken during the first and second MESSENGER flybys of Mercury on 14 January and 6 October 2008. Together with magnetic field measurements taken during the Mariner 10 flybys on 29 March 1974 and 16 March 1975, there exist three low-latitude traversals separated in longitude and one high-latitude encounter. From our model formulation and fitting procedure a Mercury dipole moment of 196 nT $\cdot R_M^3$ (where R_M is Mercury's radius) was determined. The dipole is offset from Mercury's center by 405 km in the northward direction. The dipole inclination to Mercury's rotation axis is relatively small, ~4°, with an eastern longitude of 193° for the dipole northern pole. Our model is based on the *a priori* assumption that the dipole position and the moment orientation and strength do not change in time. The root mean square (rms) deviation between the Mariner 10 and MESSENGER magnetic field measurements and the predictions of our model for all four flybys is 10.7 nT. For each magnetic field component the rms residual is ~6 nT or about 1.5% of the maximum measured magnetic field, ~400 nT. This level of agreement is possible only because the magnetospheric current system parameters have been determined separately for each flyby. The magnetospheric stand-off distance, the distance from the planet's center to the inner edge of the tail current sheet, the tail lobe magnetic flux, and the displacement of the tail current sheet relative to the Mercury solar-magnetospheric equatorial plane have been determined independently for each flyby. The magnetic flux in the tail lobes varied from 3.8 to 5.9 MWb; the subsolar magnetopause stand-off distance from 1.28 to 1.43 R_M; and the distance to the inner edge of the current sheet from 1.23 to 1.32 R_M. The differences in the current systems between the first and second MESSENGER flybys are attributed to the effects of strong magnetic reconnection driven by southward interplanetary magnetic field during the latter flyby.

1. Introduction

Magnetic field measurements in the vicinity of Mercury to date have been obtained in the course of four spacecraft flybys: two Mariner 10 flybys on 29 March 1974 (M10 I) and 16 March 1975 (M10 III), respectively, and two flybys by the MErcury Surface, Space ENvironment, GEochemistry, and Ranging (MESSENGER) spacecraft (Solomon et al., 2001) on 14 January 2008 and 6 October 2008 (M1 and M2, respectively). These measurements revealed the presence of an internal magnetic field that at Mercury's surface is about 100 times smaller than Earth's surface magnetic field (Ness et al., 1974). The higher solar wind pressure and the stronger magnitude of the interplanetary magnetic field (IMF) in the inner heliosphere combined with the relatively weak planetary field result in a magnetosphere about Mercury whose size is only about 6% that of Earth's magnetosphere (Slavin and Holzer, 1979a). The formation of the magnetosphere is associated with the flow of currents, which carry a magnetic field contribution that is superposed on the planetary magnetic field. These currents may vary between different passes or even during a single pass due to the short reconfiguration time of Mercury's magnetosphere, which is on the order of a few minutes (e.g., Slavin et al., 2007). To account for these contributions and to refine the estimate for the planetary moment, a magnetospheric magnetic field model is required. The model presented in Alexeev et al. (2008), used previously to analyze

* Corresponding author.
E-mail address: alexeev@dec1.sinp.msu.ru (I.I. Alexeev).

0019-1035/$ - see front matter © 2010 Elsevier Inc. All rights reserved.
doi:10.1016/j.icarus.2010.01.024

observations from the Mariner 10 flybys, is extended in this work to include dipole-tilt effects. The new model incorporates the newly available data from MESSENGER's first two flybys to yield better estimates of Mercury's magnetic field and to detail the effects of Mercury's magnetospheric currents.

The Mariner 10 data have been extensively analyzed over the last three decades to infer Mercury's internal field strength and configuration. Conducting a least-squares fit of the M10 I data to an offset tilted dipole, Ness et al. (1974) obtained a dipole moment of 227 nT · R_M^3, where R_M = 2439 km is Mercury's radius, and a dipole tilt angle of 10° relative to the planetary rotation axis. The dipole moment was determined to be offset by 0.45 R_M in the northward direction. This estimate of the central dipole moment was later revised to the value of 350 nT · R_M^3 (Ness et al., 1975). These authors used data only from the inbound portion of M10 I in the determination of the magnetic moment, because substorm-like magnetospheric disturbances were observed during the second half of that flyby (Siscoe et al., 1975). From the M10 III observations, Ness et al. (1976) determined a dipole moment of 342 nT · R_M^3, which is in close agreement with the revised estimate from M10 I above. Korth et al. (2004) accounted for the contribution of the external magnetic field to the observations with a modified Tsyganenko 96 model and found resulting strengths of the dipole moment ranging between 198 nT · R_M^3 and 348 nT · R_M^3, consistent with findings from other authors [see Engle (1997), in which the dipole moment estimates varied between 154 nT · R_M^3 (M10 I) and 182 nT · R_M^3 (M10 III)]. More recently, Alexeev et al. (2008) introduced a new model of Mercury's magnetosphere that was then used to determine from observations made during the two Mariner 10 flybys a Mercury magnetic dipole moment of 192 nT · R_M^3, a value within the range of estimates from previous models. This model ignored the dipole tilt angle and used both inbound and outbound observations from M10 I. The best fit to the Mariner 10 measurements yielded a dipole offset of 0.18 R_m northward of the equatorial plane (Alexeev et al., 2008). The cause for the large spread in the reported estimates of the dipole term is the limited spatial coverage of the observations, which is insufficient for separating the higher-order multipoles (Connerney and Ness, 1988), and variable magnetic field contributions from the magnetospheric current systems (Slavin and Holzer, 1979b; Korth et al., 2004).

The magnetic field strength observed by MESSENGER during M1 is consistent to within an estimated uncertainty of 10% with that during M10 I in this region (Anderson et al., 2008). Centered-dipole solutions yielded a southward planetary moment of 230–290 nT · R_M^3 tilted by 5–12° from the planetary rotation axis. These estimates lie within the uncertainty interval of Korth et al. (2004) and can be interpreted as a more precise refinement of the Mercury dipole moment after the first MESSENGER flyby.

The importance of considering the magnetic fields due to magnetospheric current systems in the estimate of the planetary magnetic moment is evident from both the Mariner 10 and MESSENGER observations, since these contributions critically affect the dipole fit estimated from spacecraft data as shown by Korth et al. (2004) and Anderson et al. (2008). These authors discussed two methods for estimating the external magnetospheric currents. The first method is based on a scaled version of a model for Earth's magnetosphere (e.g., Anderson et al., 2008): after the determination of the solar wind parameters, which are needed to calculate the external field, the external field vectors are extracted from the spacecraft data, and the residuals are fit by spherical harmonic analysis to determine the dipole terms. Alternatively, the spherical harmonic expansion series can be extended to include the external field terms so that internal and external field coefficients are fit simultaneously (Anderson et al., 2008). However, the latter approach can be used only if the magnetic field has been measured in current-free regions of the magnetosphere, a condition that is not strictly met, especially during the M10 I, M1, and M2 flybys. These flyby trajectories were located in the nightside, near-equatorial magnetosphere, placing the spacecraft within or in close proximity to the cross-tail current sheet. At Earth, the inner edge of the tail current sheet, R_2, can be usually found at R_2 = 0.7 R_1 at local midnight, where R_1 is the subsolar magnetopause distance, while at Mercury where the average $R_1 \approx 1.4\ R_M$, we typically have $R_2 \approx 1.0\ R_M$. Throughout the M10 I pass, plasma-sheet-type electron distributions were observed, with an increase in temperature beginning near closest approach coincident with a series of intense energetic-particle events (Ogilvie et al., 1977; Christon, 1987). This observation implies that the inner edge of the Mercury tail current sheet was close to the planetary surface, so a scalar potential cannot be used for the external magnetic field representation along the M10 I, M1, and M2 trajectories.

2. Methodology and fitting procedure

In this paper we employ a "paraboloid" model of Mercury's magnetosphere. The advantages of the paraboloid model are that it is a robust treatment that reproduces the main features of solar wind flow past a planetary dipole (Alexeev et al., 2003; Belenkaya, 2009). We have successfully adapted the Earth magnetospheric model to the Jupiter and Saturn magnetospheres (Alexeev and Belenkaya, 2005; Alexeev et al., 2006).

We have elected not to employ spherical harmonic analysis to find model parameters, because such analysis is most fruitful in situations where observational points are well distributed in spherical geometry, whereas magnetic field observations at Mercury are to date restricted to four spacecraft flyby trajectories. In this section, we briefly describe the paraboloid model, which includes four terms that form the magnetospheric field: (1) the eccentric dipole; (2) magnetopause currents; (3) tail currents; and (4) the penetrated IMF. The model formulation is detailed in Appendix.

The determination of the internal dipole and its higher-order terms from flyby data amounts to minimization of an objective function (such as the root mean square deviation between the data and the model) subject to the following key assumptions and/or constraints: (a) the planetary dipole is assumed to be fixed in a planetographic coordinate system, i.e., it does not change in time and is the same for all flybys; and (b) the magnetosphere may vary between different flybys in response to the different solar wind and IMF conditions but is quasi-stationary during each flyby. This latter assumption is accurate during the northward IMF conditions that prevailed during the M10 III and M1 passes, but it is clearly a simplification during southward IMF conditions (M10 I and M2) when the magnetosphere was strongly dynamic. Particularly for the M10 I flyby there is evidence that the solar wind pressure and the IMF direction changed markedly near closest approach and that magnetospheric processes similar to terrestrial substorms may have ensued (Siscoe et al., 1975). For these reasons the model parameters corresponding to the magnetopause and tail currents are considered as five separate sets of unknowns (corresponding to M10 I pre- and post-closest-approach, M10 III, M1, and M2, respectively) that are to be determined from the minimization along with the dipole terms.

The dipole field is determined by six parameters: three components of the dipole magnetic moment, M_x, M_y, M_z, and the dipole offset vector projections, dx, dy, dz. The magnetospheric current systems are determined independently for each flyby, and there are two magnetospheric states for M10 I. In addition to the six dipole parameters, the Mercury magnetospheric model field will be determined by the following nine magnetospheric parameters:

(1) the dipole tilt ψ,
(2) the magnetopause stand-off distance R_1,

Please cite this article in press as: Alexeev, I.I., et al. Mercury's magnetospheric magnetic field after the first two MESSENGER flybys. Icarus (2010), doi:10.1016/j.icarus.2010.01.024

(3) the distance R_2 to the inner edge of the tail current sheet,
(4) the tail lobe magnetic flux Φ_{lobe},
(5) the vertical displacement z_0 of the current sheet relative to the solar-magnetospheric equatorial plane,
(6) the reconnection "efficiency" k_r,
(7–9) components of the IMF vector $\boldsymbol{B}_{IMF}$.

Five of the magnetospheric parameters are determined prior to the fitting procedure. The dipole tilt is determined uniquely by Universal Time and the dipole position relative to the center of the planet. The reconnection "efficiency" coefficient is assumed equal to unity, $k_r = 1$ (Alexeev et al., 2008) in the absence of sufficient data to determine its value. The IMF vector is determined before the fitting procedure by averaging the spacecraft magnetometer data upstream of Mercury's bow shock. In our fitting procedure, the IMF vectors have no influence on magnetospheric parameters, because after finding a set of the best-fit magnetospheric parameters, we calculated the constant (but different for each magnetospheric parameter set) field vector that minimizes the average deviation vector between the model prediction and measured magnetic field.

For each magnetospheric state, seven magnetospheric parameters must be determined by the fitting procedure. They are (1) R_1, (2) R_2, (3) Φ_{lobe}, (4) z_0, and (5)–(7) the three constant components of the vector $\boldsymbol{B}_i$ that must be added to the model field so that the averaged deviation along a given trajectory equals zero. This last term can be used to estimate the magnetic field of current systems not included in our model, such as field-aligned currents and induction currents.

To determine the dipole and magnetospheric parameters, we have compiled over 1000 data points distributed among the four flybys as follows: 180 (M10 I), 149 (M10 III), 246 (M1), and 559 (M2). For Mariner 10 magnetometer data, we have used a 6-s averaging time window, and for MESSENGER data this window length was 4 s. The data points are weighted equally in the course of the fitting procedure. Where possible we have included all magnetometer observations inside the magnetosphere during each pass. During M1, the spacecraft entered the magnetosphere on the nightside of the dusk flank of the low-latitude magnetosphere within the tail current sheet, and data obtained during the inbound part of this pass and prior to MESSENGER crossing the inner edge of the tail current sheet were not used to fit our magnetospheric parameters because our model does not take into account the plasma-sheet contribution to the total pressure. A total of 41 "best-fit" parameters (six dipole parameters and five sets of the seven magnetospheric parameters for each flyby data set) are derived by minimizing the total mean square deviation between model field vectors and measured magnetic field vectors over the entire data set.

We use here the method of constrained minimization for a χ^2-like functional (Silin, 1976, 1983; Dymov et al., 2000). Following Alexeev et al. (2008), we search for the global minimum of χ^2, which depends on Mercury's dipole moment, the dipole offsets, and the parameters of the global magnetospheric current systems. Here the functional, χ^2, is

$$\chi^2 = \frac{1}{2}\sum_{i=1}^{N}\left[\mathbf{B}_{obs\_i}(\mathbf{x}_i) - \mathbf{B}_{\mathrm{mod}\_i}(\mathbf{x}_i, p_1, \ldots, p_{n_{par}})\right]^2 = \frac{1}{2}\sum_{i=1}^{N}\left[\left(B_{x\_obs\_i} - B_{x\_\mathrm{mod}\_i}\right)^2 + \left(B_{y\_obs\_i} - B_{y\_\mathrm{mod}\_i}\right)^2 + \left(B_{z\_obs\_i} - B_{z\_\mathrm{mod}\_i}\right)^2\right], \quad (1)$$

where $\mathbf{B}_{obs\_i}(\mathbf{x}_i)$ and $\mathbf{B}_{\mathrm{mod}\_i}(\mathbf{x}_i, p_1, \ldots, p_{n_{par}})$ are the vectors of the measured and model fields at the ith measured point $\mathbf{x}_i$, respectively. The model field vector, $\mathbf{B}_{\mathrm{mod}\_i}(\mathbf{x}_i, p_1, p_2, \ldots, p_{n_{par}})$, is dependent on n_{par} parameters $p_1, p_2, \ldots, p_{n_{par}}$, which determine the value of χ^2. As an indicator of the model accuracy we use a root mean square (rms) deviation:

$$\mathrm{rms} = \sqrt{\frac{\chi^2}{N - n_{par} + 1}}, \quad (2)$$

where N is the number of the measured points in the functional (1) and n_{par} is the number of parameters in the fit. Our task is to find the set of parameters p_j ($j = 1, \ldots, n_{par}$) that will determine the minimum rms value. These parameter values will correspond to the minimization of χ^2. The details of the numerical algorithm (FUMILI) used here to minimize χ^2 and of the post-processing required to ensure that we find a global minimum are discussed in Section 8.

3. Model input

3.1. Magnetic field data

The MESSENGER Magnetometer (MAG) has been described in detail by Anderson et al. (2007). The triaxial sensor is mounted at the end of a 3.6-m boom to minimize the magnitude of stray spacecraft-generated magnetic fields at the sensor location. Ground testing and in-flight calibration have shown that the intensity of uncorrectable (i.e., variable) stray fields is less than 0.1 nT (Anderson et al., 2007). While the Magnetometer is capable of measuring the full strength of the Earth's field for integration and check-out, it is designed to operate in its most sensitive field range of ±1500 nT per axis when the spacecraft is in orbit about Mercury. The 16-bit telemetered resolution yields a digital resolution of 0.05 nT. During the orbital phase of the mission, the sampling rate of the instrument will be varied according to a pre-planned schedule from 2 to 20 vectors per second. Additionally, 8-min intervals of 20-vectors-per-second burst data will be acquired during periods of lower-rate continuous sampling. The accuracy of the MESSENGER magnetic field measurements is 0.1%.

3.2. Longitudinal dependence of the four Mercury flybys

The spacecraft closest approach during each of four Mercury flybys (M10 I, M10 III, M1, and M2) maps to different Mercury longitudes, as seen in Fig. 1: ~90°E (M10 I and M10 III), ~225°E (M2), and ~45°E (M1). Similarly, the longitudes of the Sun (noon) meridian differ among the encounters: ~260° for M10 I and M10 III, 185° for M1, and 3° for M2.

This point must be taken into account to calculate the transformation matrix from Mercury solar orbital (MSO) coordinates, in which data are given, to Mercury solar-magnetospheric (MSM) coordinates, which are the model coordinates (see Appendix). The dipole offset results in a displacement of the origin, which coincides with the center of the planet for MSO coordinates and with the dipole position for MSM coordinates. Following the eccentric dipole representation of the planetary field used for Earth's magnetic field (Fraser-Smith, 1987), we will assume that the eccentric dipole direction is parallel to the tilted centered dipole.

3.3. Coordinate transformations for a tilted dipole

The magnetometer data used in the analysis presented here are those provided in MSO coordinates. In this coordinate system, the X_{MSO}-axis is directed from the center of the planet toward the Sun; the Z_{MSO}-axis is normal to Mercury's orbital plane and positive toward the north celestial pole; and the Y_{MSO}-axis completes the right-handed system. In the following we use an approximation in which Mercury's rotation axis coincides with the Z_{MSO}-axis. Fig. 2 shows the mutual orientation of the Sun–Mercury line,

Please cite this article in press as: Alexeev, I.I., et al. Mercury's magnetospheric magnetic field after the first two MESSENGER flybys. Icarus (2010), doi:10.1016/j.icarus.2010.01.024

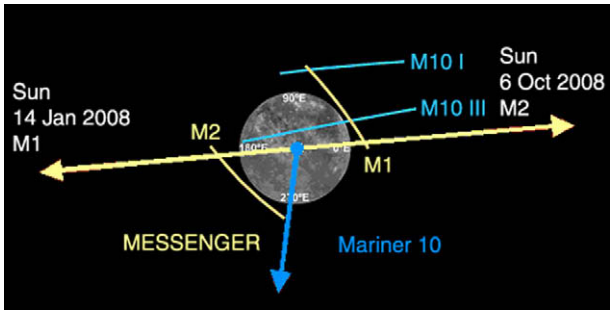

Fig. 1. Trajectories of the four Mercury flybys in MBF (planetographic) coordinates, looking down from Mercury's north pole. The yellow (MESSENGER) and blue (Mariner 10) arrows show the direction to the Sun at the time of each flyby. The noon longitudes for M10 I and M10 III were about the same and are marked by a single arrow.

Mercury's axis, and Mercury's dipole. The last vector is tilted with respect to the vertical axis of the MSM coordinate system, as described by the angle ψ between the northern magnetic pole $\boldsymbol{P_N}$ and the Z_{MSM}-axis. To transform from the MSO to the MSM system, we must make two transformations, a rotation by the angle β_3 about the X-axis and a displacement of the origin O by (dx, dy, dz). For simplicity, the origin displacement is not shown in Fig. 2. The rotation about the X_{MSO}-axis is anticlockwise for $\beta_3 > 0$. The displacement of the origin from Mercury's center (O) by (dx, dy, dz) to the shifted dipole position (O′) is shown in Fig. 3.

We note that in Fig. 2 θ_d is the magnetic pole colatitude (the angle between Mercury's dipole moment $\boldsymbol{M_d}$ and Mercury's spin axis), and λ is the angle between the noon planetographic meridian and the dipole planetographic meridian ($\lambda = \lambda_{dip} - \lambda_{Sun}$, where λ_{dip} is the planetographic longitude of the magnetic pole and λ_{Sun} is the planetographic longitude of the subsolar point).

Thus the $\boldsymbol{M_d}$ projections in the MSO coordinate system are

$$\boldsymbol{M_d} = M_d\{\sin\theta_d\cos\lambda, \sin\theta_d\sin\lambda, \cos\theta_d\}. \quad (3)$$

Below we introduce the matrix of the transformation from MSM to MSO coordinates, which takes into account the dipole offset relative the center of the planet. This matrix is shown on the left side of Eq. (4). On the right side are the transformations from MSO coordinates

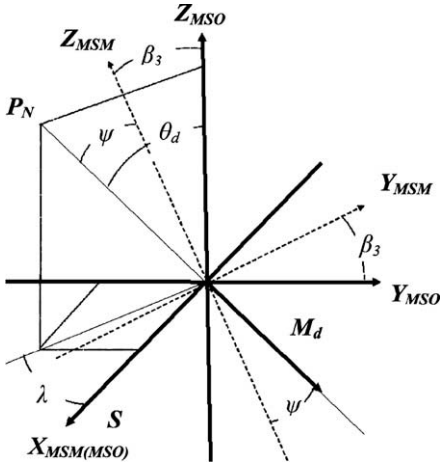

Fig. 2. Illustration of some geometric parameters, including the magnetic dipole moment $\boldsymbol{M_d}$, the dipole northern pole colatitude θ_d, the angle $\lambda = \lambda_{dip} - \lambda_{Sun}$ between the dipole northern pole ($\boldsymbol{P_N}$) longitude and the longitude of noon, the rotation angle β_3, and the dipole tilt angle ψ. The X_{MSO}, Y_{MSO}, and Z_{MSO} axes are shown by solid arrows, and the Y_{MSM} and Z_{MSM} axes are shown by dotted arrows; the Mercury dipole magnetic moment is marked by a bold solid arrow. For simplicity we do not show here the origin displacement.

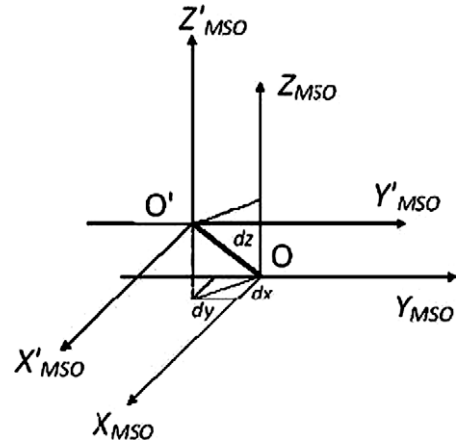

Fig. 3. The displacement of the origin from Mercury's center (O) to the shifted dipole position (O′).

to the Mercury body-fixed (MBF) or planetographic coordinate system, which are equivalent to rotation about Mercury's spin axis by an angle λ_{Sun}. Because of Mercury's rotation, the angles ψ and β_3 have different values during each of the flybys given the fixed dipole position relative to the planet body.

$$\begin{aligned} &x_{MSO} = x_{MSM} - dx, \quad x_{MBF} = x_{MSO}\cos\lambda_{Sun} - y_{MSO}\sin\lambda_{Sun},\\ &y_{MSO} = y_{MSM}\cos\beta_3 - z_{MSM}\sin\beta_3 - dy, \quad y_{MBF} = x_{MSO}\sin\lambda_{Sun} + y_{MSO}\cos\lambda_{Sun},\\ &z_{MSO} = y_{MSM}\sin\beta_3 + z_{MSM}\cos\beta_3 - dz, \quad z_{MBF} = z_{MSO}. \end{aligned} \quad (4)$$

The best-fitting values for dipole inclination angle (about 3.9°) and the dipole offset for all four flybys are given in Table 1. The table also gives the dipole tilt angle with respect to the Z_{MSM}-axis of MSM coordinates and the rotation angle β_3 of the YZ plane. The latitude and longitude of the northern magnetic pole in Mercury planetographic coordinates have been determined by a fitting procedure that is described below. The dipole offsets in the same coordinate system have been determined simultaneously. Consider the solid triangle $\boldsymbol{P_N Z_{MSM} Z_{MSO}}$ in which two dihedral angles are known, $\boldsymbol{Z_{MSM}}$ and $\boldsymbol{Z_{MSO}}$; these are equal to 90° ($\boldsymbol{Z_{MSM}}$) and to 90° − λ ($\boldsymbol{Z_{MSO}}$), respectively. The three arcs in this solid triangle are β_3, θ_d, and ψ. From spherical trigonometric relations for the solid triangle $\boldsymbol{P_N Z_{MSM} Z_{MSO}}$:

$$\begin{aligned} &\frac{\sin\theta_d}{\sin 90^\circ} = \frac{\sin\psi}{\cos\lambda}, && \sin\psi = \sin\theta_d\cos\lambda,\\ &\cos\theta_d = \cos\beta_3\cos\psi + \sin\beta_3\sin\psi\cos 90^\circ, && \cos\theta_d = \cos\beta_3\cos\psi,\\ &\cos\psi = \cos\beta_3\cos\theta_d + \sin\beta_3\sin\theta_d\sin\lambda, && \cos\psi = \cos^2\beta_3\cos\psi + \sin\beta_3\sin\theta_d\sin\lambda,\\ & && \cos\psi\sin^2\beta_3 = \sin\beta_3\sin\theta_d\sin\lambda. \end{aligned} \quad (5)$$

Finally, to calculate β_3 and ψ:

$$\begin{aligned} &\sin\psi = \sin\theta_d\cos\lambda, && \cos\psi = \frac{\cos\theta_d}{\cos\beta_3},\\ &\sin\beta_3 = \frac{\sin\theta_d\sin\lambda}{\cos\psi}, && \tan\beta_3 = \tan\theta_d\sin\lambda. \end{aligned} \quad (6)$$

After computation of the angle β_3 for each flyby, we calculated the dipole offsets in MSM coordinates, Δx_d, Δy_d, Δz_d, which will be used to model magnetic field calculations. The values (in R_M) are shown in Table 1. Vertical displacements of the tail current sheet relative to the equatorial plane, z_0 (in R_M), and the polar cap size, $_{pc}$ (in degrees), are also shown in the table.

4. Model–data comparison: overview of Mariner 10 and MESSENGER data

The magnetic field observations by Mariner 10 and MESSENGER are compared with the best-fit model field, consisting of the best-fitting dipole (Table 2) and paraboloid model parameters (Table 3) in Fig. 4. In the fitting procedure, a single set of dipole parameters

Please cite this article in press as: Alexeev, I.I., et al. Mercury's magnetospheric magnetic field after the first two MESSENGER flybys. Icarus (2010), doi:10.1016/j.icarus.2010.01.024

Table 1
Values of the dipole tilt, offsets of dipole and cross-tail current sheet, and polar cape size derived from the fit procedure.

Flyby	ψ, deg	β_3, deg	Δx_d, R_M	Δy_d, R_M	Δz_d, R_M	z_0, R_M	θ_{pc}, deg
M10 I in	1.5	−3.6	−0.023	−0.040	0.164	0.04	56
M10 I out	1.5	−3.6	−0.023	−0.040	0.164	0.38	64
M10 III	1.6	−3.6	−0.022	−0.041	0.164	−0.83	48
M1	3.8	0.6	0.024	−0.028	0.167	0.02	46
M2	−3.8	−0.7	−0.024	0.027	0.167	−0.12	46

was fit to all five data sets. For all flybys the spacecraft entered the magnetosphere through the dusk flank and exited the magnetosphere through the dawn flank (from right to left in Fig. 4). The M2 outbound crossing almost coincided with the maximum in the measured magnetic field strength that was identified as a large flux transfer event (Slavin et al., 2009b). The magnetopause crossing positions shown in this figure are determined by the subsolar distances to the modeled parabolic magnetopause. (Note that the model fits indicated by the bold lines incorporate only those points that lie inside the magnetosphere.) The general agreement between the observed outbound crossings and the model magnetopause positions supports the model fitting results.

As can be seen in Fig. 5, the outbound magnetopause crossings for M10 I and for both MESSENGER flybys occurred for x_{MSM} close to zero, near the dawn flank of the terminator magnetopause intersection and nearly on the MSM equatorial plane during the MESSENGER encounters. For each flyby the MSM equatorial plane has a small inclination, the angle β_3 in Eq. (5), to Mercury's orbital plane (the plane $z_{MSO} = 0$ in MSO coordinates), and these inclinations are different for each flyby.

For the M10 I outbound magnetopause crossing, z_{MSM} is about 0.5 R_M. For all three passes the observed magnetopause coordinates that can be determined from the magnetometer data and paraboloid model predictions are in good agreement. For M1 and M2 the magnetospheric fields at the magnetopause are significantly higher (by factors of 2–3) than the IMF strength upstream of the bow shock. In these cases we have a well-defined magnetopause.

The positions of the spacecraft trajectories relative to the equatorial plane depend on the dipole offset, the dipole moment direction, and the location of the magnetic poles on Mercury's surface. All these parameters have been calculated from results of the fitting procedure by comparing the model prediction and the measured magnetic field vectors. The projections of the flyby trajectories onto the terminator plane ($x_{MSM} = 0$) and onto the noon–midnight plane ($y_{MSM} = 0$) are shown in Fig. 6. During M2 the MESSENGER trajectory was close to but south of the MSM equatorial plane and also close to and south of the plane of the tail current sheet. During M1 the MESSENGER trajectory was also close

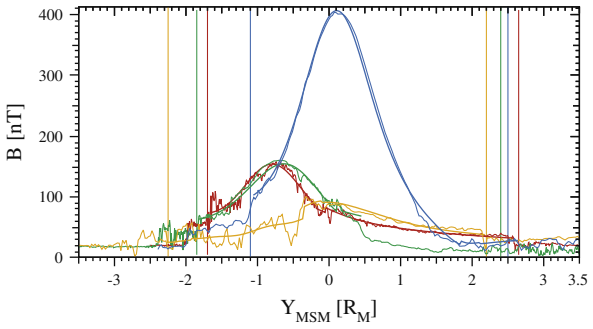

Fig. 4. A comparison of the magnetometer data (dashed) and magnetic field strength predicted by the best-fit model (solid) for M10 I (orange curves), M10 III (blue), M1 (green), and M2 (red). For each flyby, thin lines represent the measured magnitudes of the magnetic field, and thick curves show the model magnetic field, both plotted as a function of the y_{MSM} solar-magnetospheric coordinate. The y_{MSM} coordinates of the paraboloid magnetopause crossings for each pass, both inbound and outbound, are indicated by colored vertical thin lines. During the flybys MESSENGER and Mariner 10 crossed Mercury's magnetosphere in the direction from dusk to dawn.

to and south of the MSM equatorial plane, but as will be discussed below the M1 trajectory likely passed inside the tail current sheet. The B_x components of the measured and model magnetic field are negative for all MESSENGER passes.

5. MESSENGER's second flyby: effects of magnetospheric currents

A comparison of the magnetic field measured by MESSENGER during M2 with the best-fitting model field is shown in Fig. 7. To fit the dipole and magnetospheric parameters, we have used Magnetometer data only from inside the magnetosphere. The inbound and outbound magnetopause crossings were at 08:11:57 and 08:49:11 UTC, respectively (Slavin et al., 2009b). The spatial dependence of the magnetic field strength within the magnetosphere is well described by the model. Major contributions to the rms discrepancy, 8.8 nT, are the quasi-periodic oscillations observed near the entry of the MESSENGER spacecraft into the magnetosphere. The amplitude of these oscillations is about 3–5 nT, and the period is ~45 s. Within this time interval the spacecraft displacement along the dawn–dusk direction is about 211 km. Additional contributions to the discrepancy between model and data are the six isolated large-amplitude short-timescale variations shown in Fig. 7b. These fluctuations have approximately the same temporal and spatial scales as the quasi-periodic oscillations but exhibit amplitudes about five times higher (about 20 nT). The biggest impulse in the magnetic field was observed near the noon–

Table 2
Dipole moment, dipole offset values, and northern pole latitude and longitude (in MBF system) fit to observations from all four flybys.

M_d, nT R_M^3	Δx_d, R_M	Δy_d, R_m	Δz_d, R_M	Θ_{nd}, deg	λ_{nd}, deg	N	σ, nT
196.0 ± 0.3	−0.026 ± 0.001	0.027 ± 0.001	0.166 ± 0.001	3.9 ± 0.1	193.3 ± 1.8	1134	10.72

Table 3
Magnetospheric current system parameters.

Flyby	R_1, R_M	R_2, R_M	Φ_{lobe}, MWb	z_0, R_M	b_x, nT	b_y, nT	b_z, nT	σ_i, nT	σ_i, nT
M10I in	1.28 ± 0.03	1.23 ± 0.01	5.08 ± 0.01	0.04 ± 0.01	33.0 ± 1.2	−4.8 ± 0.4	25.8 ± 1.1	14.9	10.7
M10I out	1.36 ± 0.02	1.32 ± 0.01	5.92 ± 0.01	0.38 ± 0.01	−34.2 ± 0.7	−12.0 ± 0.3	22.1 ± 1.2	14.9	10.7
M10 III	1.43 ± 0.01	1.25 ± 0.01	4.06 ± 0.01	−0.83 ± 0.01	28.3 ± 0.4	−2.3 ± 0.2	27.8 ± 1.0	11.7	10.7
M1	1.35 ± 0.01	1.32 ± 0.01	3.83 ± 0.01	−0.02 ± 0.01	6.7 ± 0.4	3.0 ± 0.1	13.4 ± 0.1	10.8	10.7
M2	1.40 ± 0.01	1.31 ± 0.01	3.83 ± 0.01	−0.12 ± 0.01	2.0 ± 0.2	1.6 ± 0.1	3.0 ± 0.02	8.9	10.7

Please cite this article in press as: Alexeev, I.I., et al. Mercury's magnetospheric magnetic field after the first two MESSENGER flybys. Icarus (2010), doi:10.1016/j.icarus.2010.01.024

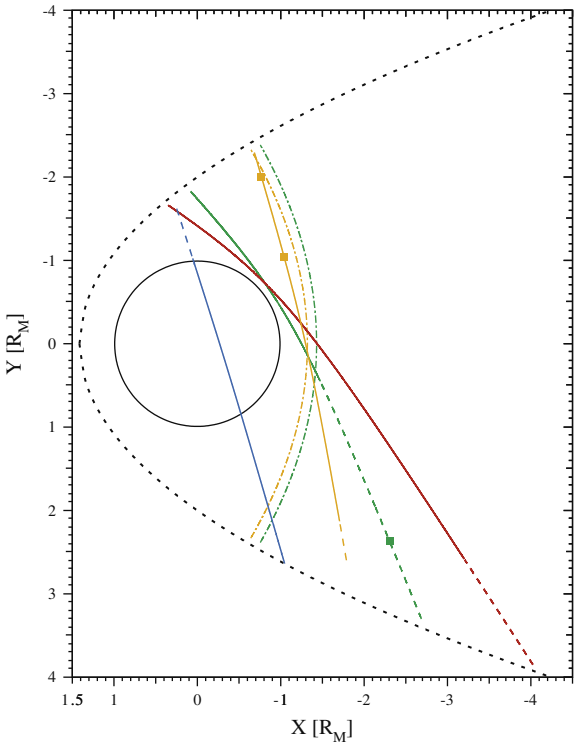

Fig. 5. Projections of the M10 I (yellow curve), M10 III (blue), M1 (green), and M2 (red) trajectories onto the solar-magnetospheric equatorial plane. For all trajectories the spacecraft traverses the magnetosphere from dusk ($Y > 0$) to dawn ($Y < 0$). Solid curves mark the portions of each trajectory from which observations were used to fit the model parameters; dashed lines mark portions of each trajectory for which magnetometer data were not included in the fitting process. The colored squares denote crossings of the current-sheet plane in the tail of the magnetosphere. The dotted black curve shows the modeled paraboloid magnetopause for an "average" magnetospheric state. Dotted color curves denote the inner edge of the tail-current sheet position for M10 I (yellow) and M1 (green).

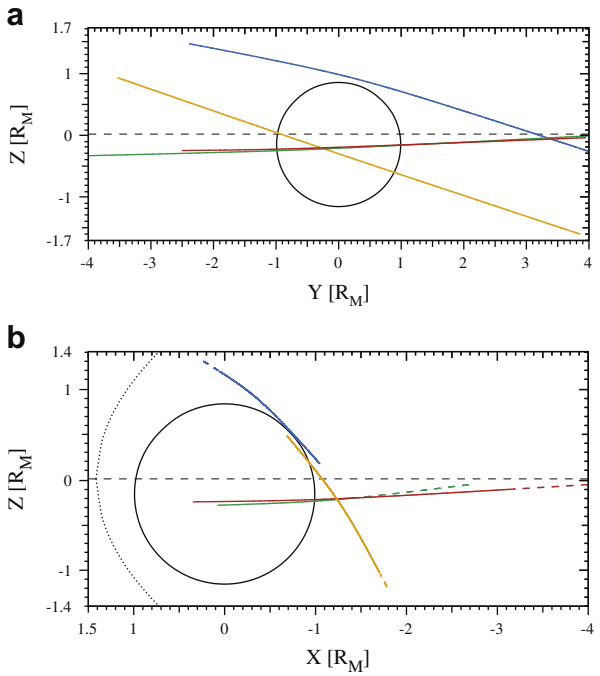

Fig. 6. Projections of the M10 I (yellow curve), M10 III (blue), M1 (green), and M2 (red) trajectories (a) onto the Mercury solar-magnetospheric terminator plane (YZ plane) and (b) onto the Mercury solar-magnetospheric noon–midnight plane (X–Z plane). For all trajectories the spacecraft traverses the magnetosphere from dusk ($Y > 0$) to dawn ($Y < 0$). The black circle denotes Mercury's cross-section; the circle's center is shifted by $\Delta z_d = 0.166\ R_M$ southward from the equatorial plane.

midnight plane ($y_{MSM} = -1.4$). The deviation in the B_x component is smaller than 2 nT, the B_y component increases by 9 nT, and the B_z component decreases by 18 nT. Similar magnetic perturbations can be produced by a strong current in the dawn–dusk direction with an inclination of 26° to the equatorial plane.

The individual magnetic field components respond differently to the dipole field and the global magnetospheric current system parameters. For the inbound pass, after MESSENGER entered the dusk flank of the magnetosphere, the B_x component is mainly determined by the tail current. Exiting the tail current sheet, the magnetic field observations in the dawnside magnetosphere are dominated by the dipole term. The B_y component is mainly controlled by the dipole field outside the tail-current-sheet region. The discrepancy in the B_y component in the tail region can be explained by greater flaring of the paraboloid magnetopause in this region compared to a real cylindrical-like tail magnetopause. On the inbound pass of the M2 trajectory (near the tail current sheet), the B_z component of the measured field is close to the dipole field. Here the magnetopause current and tail current contributions to the B_z component cancel each other. After MESSENGER entered the inner magnetosphere, the observed B_z component was as much as 20–30 nT less than the modeled dipole field. In this region the negative tail current contribution is larger than that from the positive magnetopause current field. The maximum of the B_z component of the dipole term is +125 nT, the tail current contribution maximum is about two times smaller in amplitude at −50 nT, and the magnetopause current brings +32 nT at the boundary between the dawn flank of the magnetosphere and the magnetosheath, nearly compensating the tail current contribution at this region. The resulting model field, B_m, is equal to the dipole B_z component and is about 100 nT. The modeled magnetospheric field at the subsolar magnetopause, B_{ms} (see Section 10), is about two times larger. The ratio of these values determines the inclination angle of the magnetopause normal to the Sun–Mercury line as $\xi \sim 35°$ (where $\sin \xi = B_m/B_{ms}$) at the point of the M2 outbound magnetopause crossing.

6. MESSENGER's first flyby: magnetospheric current contributions

MESSENGER's first two flybys of Mercury had similar trajectories (except that the longitudinal sectors in MBF coordinates were nearly opposite to each other). Both trajectories had a small inclination to the MSM equatorial plane and crossed the magnetosphere from dusk to dawn. The M1 and M2 closest approach (CA) positions occurred at the about the same point ($x_{MSM} = -0.7$, $y_{MSM} = -0.7$, and $z_{MSM} = -0.2$, all in R_M). During M2 the spacecraft entered the magnetosphere tailward of the M1 entry by ~0.7 R_M and exited the magnetosphere closer to the nose than during M1. For this reason the M1 and M2 magnetic field profiles are similar in many respects, including the measured peak magnetic field intensity. Prior to CA the field measured during M2 (Fig. 4) was lower than during M1 by about 10–12 nT at a given Y_{MSM} coordinate, because this portion of the M1 trajectory was closer to Mercury than the equivalent portion of the trajectory during M2. However, at $x_{MSM} = -1.5\ R_M$ and $y_{MSM} = 0.5\ R_M$ the field measured during M1 was sharply reduced, and on its inbound pass the field measured during M1 was about 20 nT weaker than during M2. This observation can be explained in one of two ways: (1) there could be some current disruption that occurred during M1 or (2) the observed variations in the magnetospheric field could reflect a strong spatial dependence of the magnetospheric field on z_{MSM}.

Please cite this article in press as: Alexeev, I.I., et al. Mercury's magnetospheric magnetic field after the first two MESSENGER flybys. Icarus (2010), doi:10.1016/j.icarus.2010.01.024

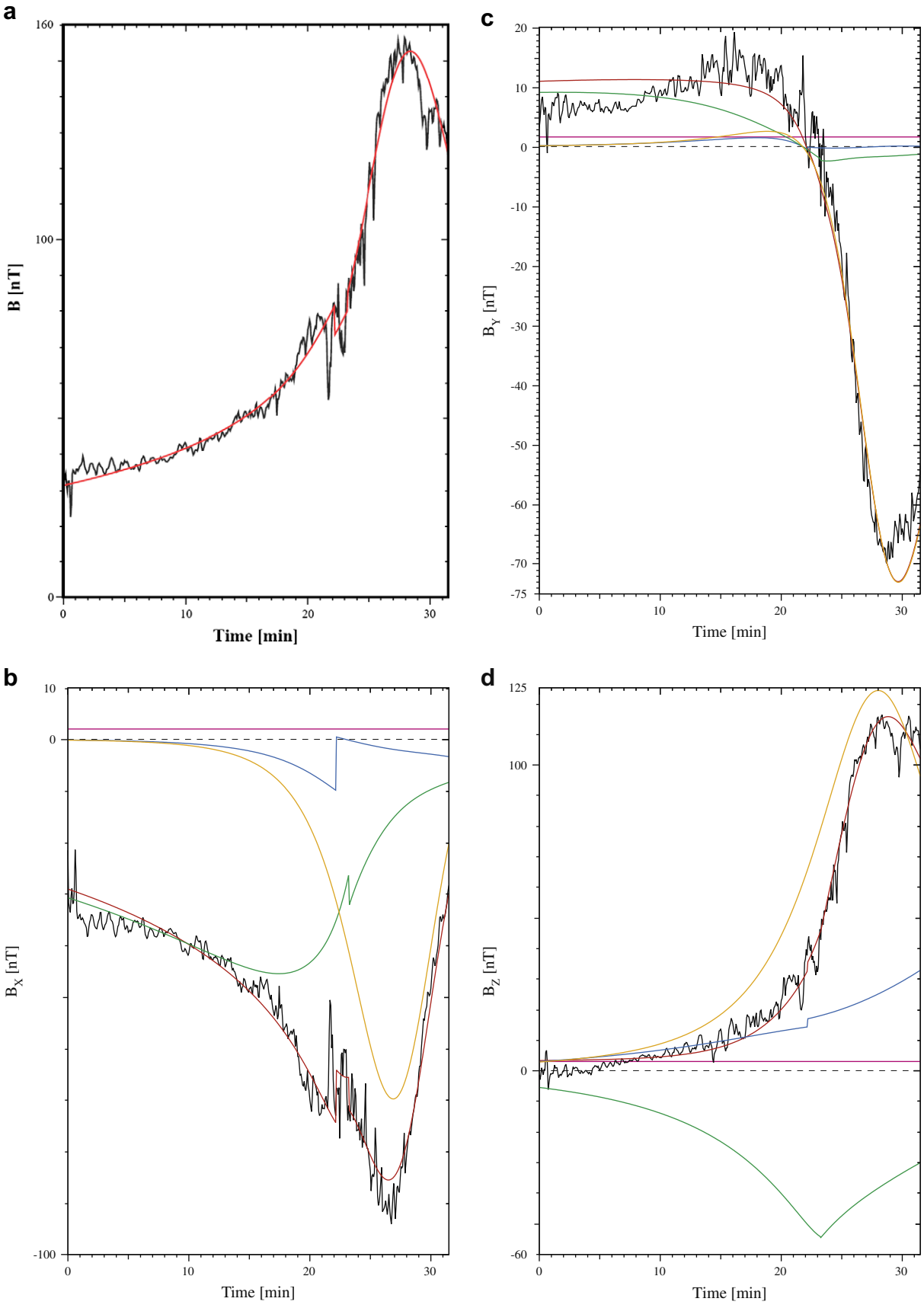

Fig. 7. Comparison of measured (black) and model (red) magnetic field during M2. (a) Scalar magnetic field strength. (b) *X* components. (c) *Y* components. (d) *Z* components. The horizontal axis shows time in minutes from the point that the spacecraft entered the magnetosphere. The contributions of the magnetopause current (blue), the tail current field (green), and the dipole term (orange) are shown in (b–d).

Please cite this article in press as: Alexeev, I.I., et al. Mercury's magnetospheric magnetic field after the first two MESSENGER flybys. Icarus (2010), doi:10.1016/j.icarus.2010.01.024

The Z_{MSM} coordinates for both encounter trajectories are close to each other, but their paths relative to the tail current sheet appear to be different. We speculate that during M1 the spacecraft may have passed inside the tail current sheet. In contrast, during M2 MESSENGER passed south of the tail current and measured only the southern lobe magnetic field.

Alternatively, the spatial variations in a steady magnetospheric field can be interpreted as long-term changes in the topology of the interior planetary magnetic field. In our approach, a longitudinal variation in the interior magnetic field can give rise to a displacement of the dipole from the origin within the equatorial plane. Our best-fitting dipole parameter values, however, show only a small (less than 100 km) dipole displacement in the equatorial plane. The second aspect of the proposition (spatial variation in a steady magnetosphere current) is supported by our best-fit magnetospheric parameter values. More clear differentiation between magnetospheric and interior magnetic field contributions can be made when magnetic field data from the orbital phase of the MESSENGER mission become available.

This discussion of the M1 inbound data illustrates the limitations of the M1 magnetic field observations as constraints on the internal magnetic field. In our fitting procedure we have therefore used data only from the second half of the M1 trajectory, during which the spacecraft was located inside the magnetosphere but outside the current sheet. We limited ourselves by the spatial interval when spacecraft coordinates were $x_{MSM} > -1.5\ R_M$ and $y_{MSM} < 0.5\ R_M$. Future work should include a plasma-sheet current model that takes into account the finite thickness of the current sheet, so that the deficit of the magnetic pressure inside the current sheet will be balanced by plasma pressure.

After limiting the portion of the M1 trajectory to the inner magnetosphere, the best-fit dipole parameters achieved a good fit (see Fig. 8). In general, the dipole moment estimates are very stable. The dipole moment compares well to results from previous analyses (e.g., Anderson et al., 2008, 2010) and is similar to estimates obtained by other methods (e.g., Slavin et al., 2009a). The northward dipole offset reported by Bergan and Engle (1981), 0.17 R_M, is very close to our estimate, 0.166 R_M (see Section 8). Similar to the case for M2, the B_y component is weakly dependent on the magnetospheric contributions, and indeed these data can be used to define dipole moment (see Fig. 8c). Only at the outbound magnetopause crossing does the Chapman–Ferraro current contribute 7 nT, about half of the total measured field (~15 nT). Near CA the dipole term is −65 nT, and other terms are less than 5 nT. For the B_x component, the magnetospheric terms provide significant contributions (see Fig. 8b), especially near the inner edge of the tail current sheet, where this term (~50 nT) is about 2.5 times larger than the dipole contribution (~20 nT). Ignoring the magnetospheric contributions results in a deviation of the model prediction from the measured field of about 15 nT, or 1.5 times more than the rms error from our fitting procedure.

It is important to emphasize that for M1 the magnetopause and tail current contributions have the same sign for B_x. Most critical to the outer (magnetospheric) terms is the B_z component of the magnetic field (see Fig. 8d), consisting predominantly of the sum of the planetary dipole and magnetopause current fields, which are both directed northward near the magnetopause inside the magnetosphere. The tail current field has a negative contribution to the total magnetospheric field, and near CA it contributes about −50 nT (compared to ~25 nT for the magnetopause-penetrated IMF terms).

The magnetic field variations at the M1 inbound magnetopause crossing indicate that the spacecraft entered through the dusk flank of the tail into the central plasma sheet just north of the mid-plane of the cross-tail current sheet (Slavin et al., 2008). As the spacecraft approached the planet, the magnetic field intensity increased as MESSENGER entered the region dominated by the dipolar planetary magnetic field (Anderson et al., 2008). The significant tailward tilting of magnetic field even close to the planet is due to the presence of a strong cross-tail current sheet. A strong magnetic field decrease, beginning at 19:10:35, corresponds to a current layer perpendicular to the magnetic field as evident by the minimal rotation in direction.

7. Deviations between model predictions and measured magnetospheric field components, M1 and M2

We now interpret the differences between the magnetic field components predicted by the best-fitting model and those measured by the MESSENGER Magnetometer, plotted versus y_{MSM} for both M1 and M2 in Fig. 9. These residuals can be used to improve the global magnetospheric current model by changing the dependence on the spatial coordinates or model parameters. Boardsen et al. (2009) recently reported the observation of ultra-low-frequency (ULF) waves at a frequency of ~0.5 Hz during M1. With the 6-s averaged data, we consider lower-frequency oscillations. We begin this analysis with data from the M2 inbound pass where MESSENGER was located in the tail lobe region just below the tail current sheet. MESSENGER's velocity during that flyby was about 5.8 km/s. A time variation in the magnetic field with a duration of about 30 s corresponds to a spatial scale of about 174 km (0.07 R_m). Quasi-periodic disturbances with a similar scale were observed by MESSENGER over the interval $2.1 > y_{MSM} > 1.5$ (see Fig. 10). That all three magnetic field components showed deviations over the same spatial interval ($y_{MSM} \sim 2.1 - 1.5\ R_m$) probably indicates that some global-scale current system has not been taken into account in our model, or that the shapes and intensities of the current systems assumed are not precisely correct. The magnitude of this shift, however, about 7 nT across 3 R_m, is sufficiently small to be ignored.

In addition to effects discussed previously, there are differences between the model and the data on shorter timescales. We note six such events in the inner magnetosphere outside of the tail-current-sheet region. The duration of these excursions of the magnetospheric field vector is about 1 min, and the amplitude is about 15 nT. Examples of these types of deviations seen between the model and data along the M1 and M2 trajectories are shown in Fig. 10. One example (Fig. 10a) can be interpreted as a non-linear Alfvénic soliton or a local current line along the dawn–dusk (y) direction. The field vector returned to the initial direction after the excursion, and the dB_y component hardly changed. The second example (Fig. 10b) corresponds to an X-directed current sheet superposed on small-scale field fluctuations.

8. Best-fit magnetic dipole based on minimization of χ^2

To determine the best-fit model parameters, which minimize the mean squared deviation between the model field vector and the measured magnetic field, we used the FUMILI code (Silin, 1976). In the high-energy accelerator physics community this code is widely used to extract the energy, mass, and impulse of energetic charged particles from tracking detector coordinate information (e.g., Silin, 1983). Detailed descriptions of this algorithm are given by Dymov et al. (2000).

In this paper we used a renewed realization of constrained minimization for χ^2-like functionals, FUMILIM (Sitnik, 2008). The algorithm of the FUMILI code was available for users as a part of the CERN library (Silin, 1983). We briefly describe the FUMILI algorithm.

As a minimum condition on χ^2, Silin (1983) used the general equation:

Please cite this article in press as: Alexeev, I.I., et al. Mercury's magnetospheric magnetic field after the first two MESSENGER flybys. Icarus (2010), doi:10.1016/j.icarus.2010.01.024

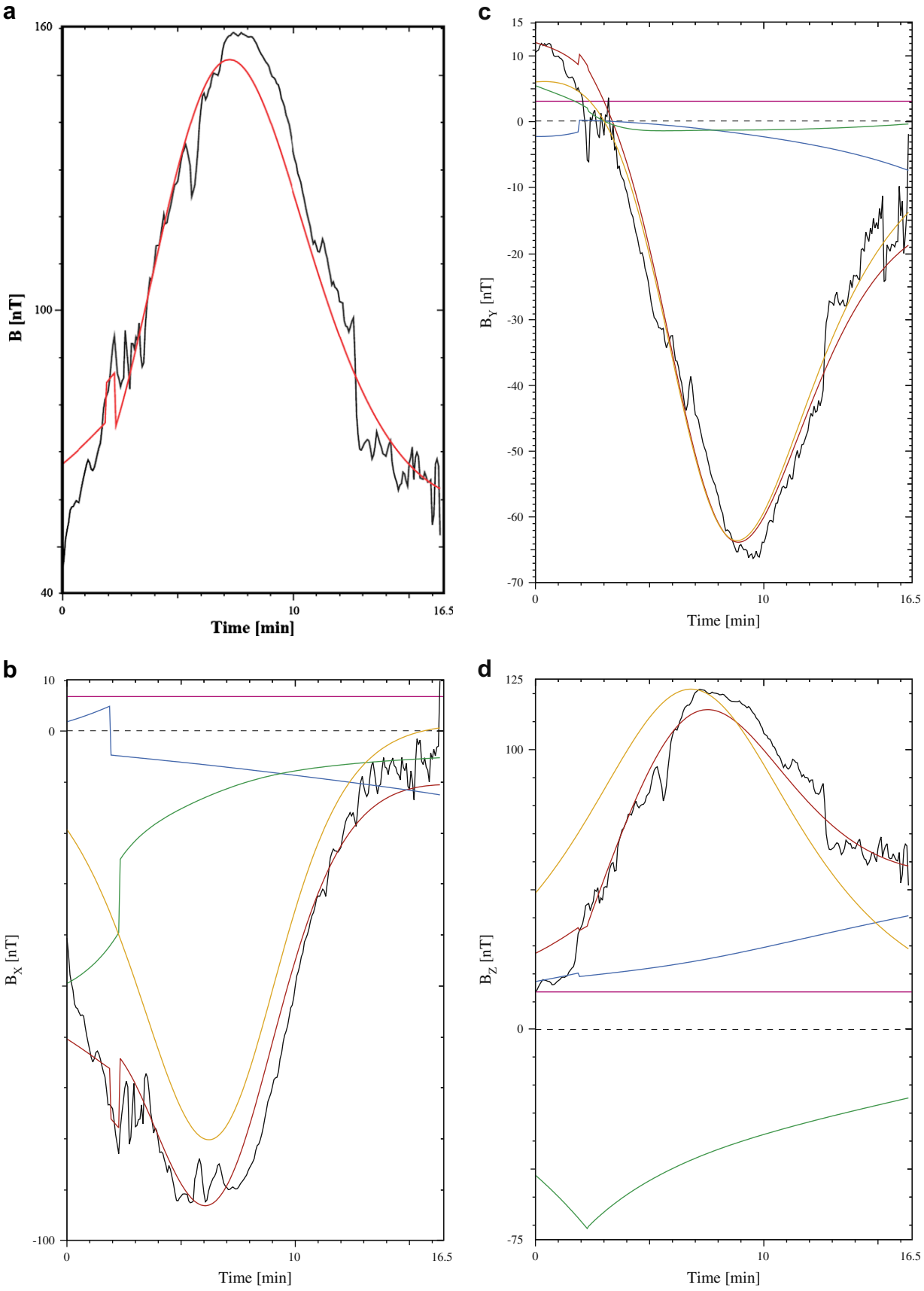

Fig. 8. Comparison of measured (black) and model (red) magnetic field during M1. (a) Scalar magnetic field strength. (b) *X* components. (c) *Y* components. (d) *Z* components. The contributions of the magnetopause current (blue), tail current field (green), and dipole term (orange) are shown in (b–d).

Please cite this article in press as: Alexeev, I.I., et al. Mercury's magnetospheric magnetic field after the first two MESSENGER flybys. Icarus (2010), doi:10.1016/j.icarus.2010.01.024

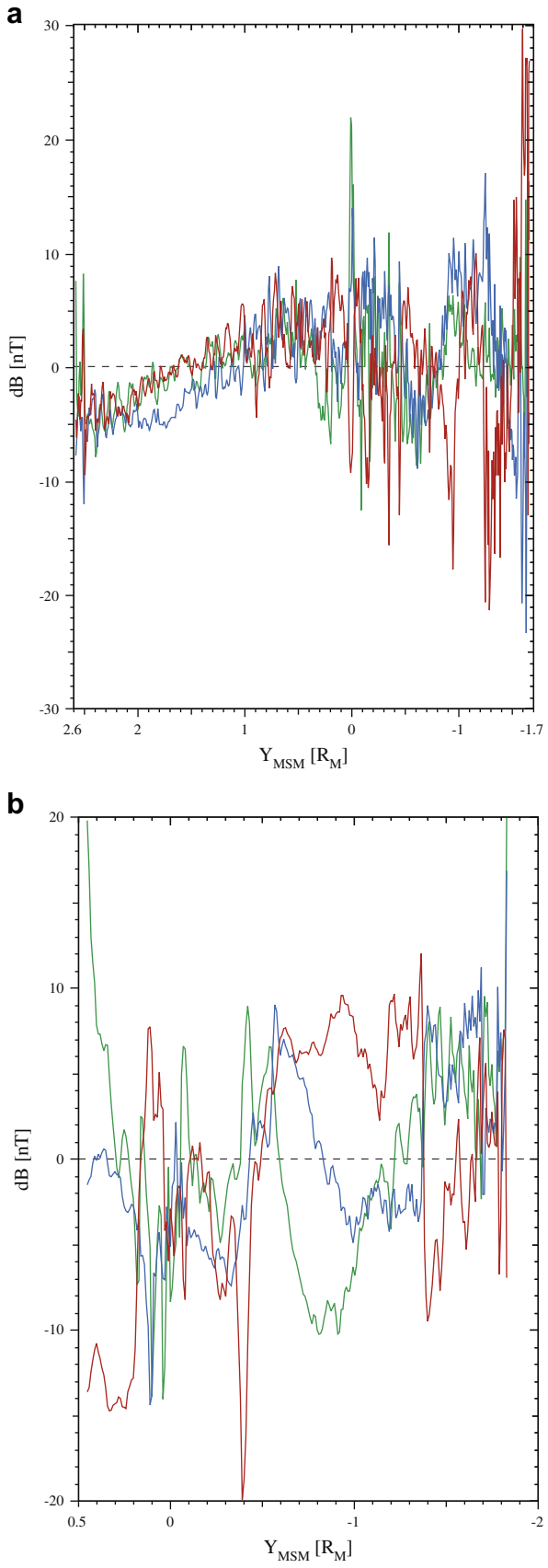

Fig. 9. Deviations between model and measured magnetospheric field components along the M1 (right) and M2 (left) trajectories. dB_x, dB_y, and dB_z are shown in and green, blue, and red, respectively.

$$\frac{\partial \chi^2}{\partial \theta_i} = \sum_{j=1}^{N} \frac{1}{\sigma_j^2} \frac{\partial f_j}{\partial \theta_i} f_j(x_j, \theta_i) = 0, \quad i = 1, \ldots, m, \tag{7}$$

where $\chi^2 = \frac{1}{2}\sum_{j=1}^{N} \frac{f_j^2(x_j,\theta_i)}{\sigma_j^2}$, and N is the total number of the measured points. At each jth point, x_j, the measured function f_j is determined by m parameters, θ_i. In our case, the function f_j is the difference between model predictions and observations:

$$f_j = \left(\boldsymbol{B}_{j\_obs} - \boldsymbol{B}_{j\_\mathrm{mod}}\right)^2 = \Delta B_i^2$$
$$= \left(B_{x\_obs} - B_{x\_\mathrm{mod}}\right)^2 + \left(B_{y\_obs} - B_{y\_\mathrm{mod}}\right)^2 + \left(B_{z\_obs} - B_{z\_\mathrm{mod}}\right)^2. \tag{8}$$

The experimental errors we adopted are small (0.1 nT) compared with the values of the deviations and are taken to be the same at each point. So we assign the statistical weight $\sigma_j = 1$ for each point. To find the solution of Eq. (7) the derivative of χ^2 is numerically calculated, and linearity of the functional nearest to the solution region is assumed. The validity of the solution was checked by calculating the deviation of the rms value from the minimum value. Here the rms deviation is

$$\mathrm{rms} = \sqrt{\frac{\chi^2}{N - m + 1}}. \tag{9}$$

The dependence of the differences $\delta_{\mathrm{rms}} = \mathrm{rms} - \mathrm{rms}_{min}$ on the dipole equatorial field strength B_d (vertical axis) and the dipole vertical offset dz is shown in Fig. 11a. It is seen that a deviation of 5% from the optimal B_d value increased the rms by a factor of ~2 ($\delta_{\mathrm{rms}} \sim \mathrm{rms}_{min}$). A similar increase in rms occurs if we change the vertical dipole offset dz by 25%, from 0.17 R_M to 0.21 R_M or 0.12 R_M, corresponding to displacement of the dipole by ~100 km along the spin axis. Contours of δ_{rms} versus B_d and dz are shown in Fig. 12. For other parameters the functional dependence of the rms misfit can be more irregular than for B_d or dz. An example, shown in Fig. 11b, is the dependence of δ_{rms} on B_d and dy. Because the displacement of the dipole in the y direction has a small influence on the dipole field contribution to the total field, changing dy mainly changes the magnetopause position at the MESSENGER or Mariner 10 trajectories. As a result, a sharp increase in rms can occur because some magnetosheath observations are then included in the data sets to be fit.

The best-fitting dipole parameters and the magnetospheric model parameters, determined from 1134 data points from all four flybys (Fig. 5), are given in Tables 2 and 3. For each vector component the residual rms deviation will be $\sigma \cdot 3^{-1/2}$; for rms = 10.72 nT, it is 6.17 nT.

9. Discussion

To compare our results on Mercury's internal field with the spherical harmonic expansion reported by Anderson et al. (2010) and Uno et al. (2009), we use the spherical harmonic expansion of the potential of a shifted dipole. An eccentric dipole representation of the planetary field was used for Earth's magnetic field by Fraser-Smith (1987). Northward displacement of Mercury's dipole (0.17 R_M) is about a factor of six greater than the dipole shifts in the equatorial plane (0.03 R_M). For simplicity we give the formula for an axial symmetric field with $dx = dy = 0$ (see Fig. 13). We also ignore the dipole tilt angle because it is small (about 4°).

We use a determination of the generating (course-of-value) function of the Legendre polynomial:

$$\frac{1}{\sqrt{1 + s^2 - 2s\cos\theta}} = \sum_{n=0}^{\infty} s^n P_n(\cos\theta) \quad \text{for } s < 1. \tag{10}$$

Please cite this article in press as: Alexeev, I.I., et al. Mercury's magnetospheric magnetic field after the first two MESSENGER flybys. Icarus (2010), doi:10.1016/j.icarus.2010.01.024

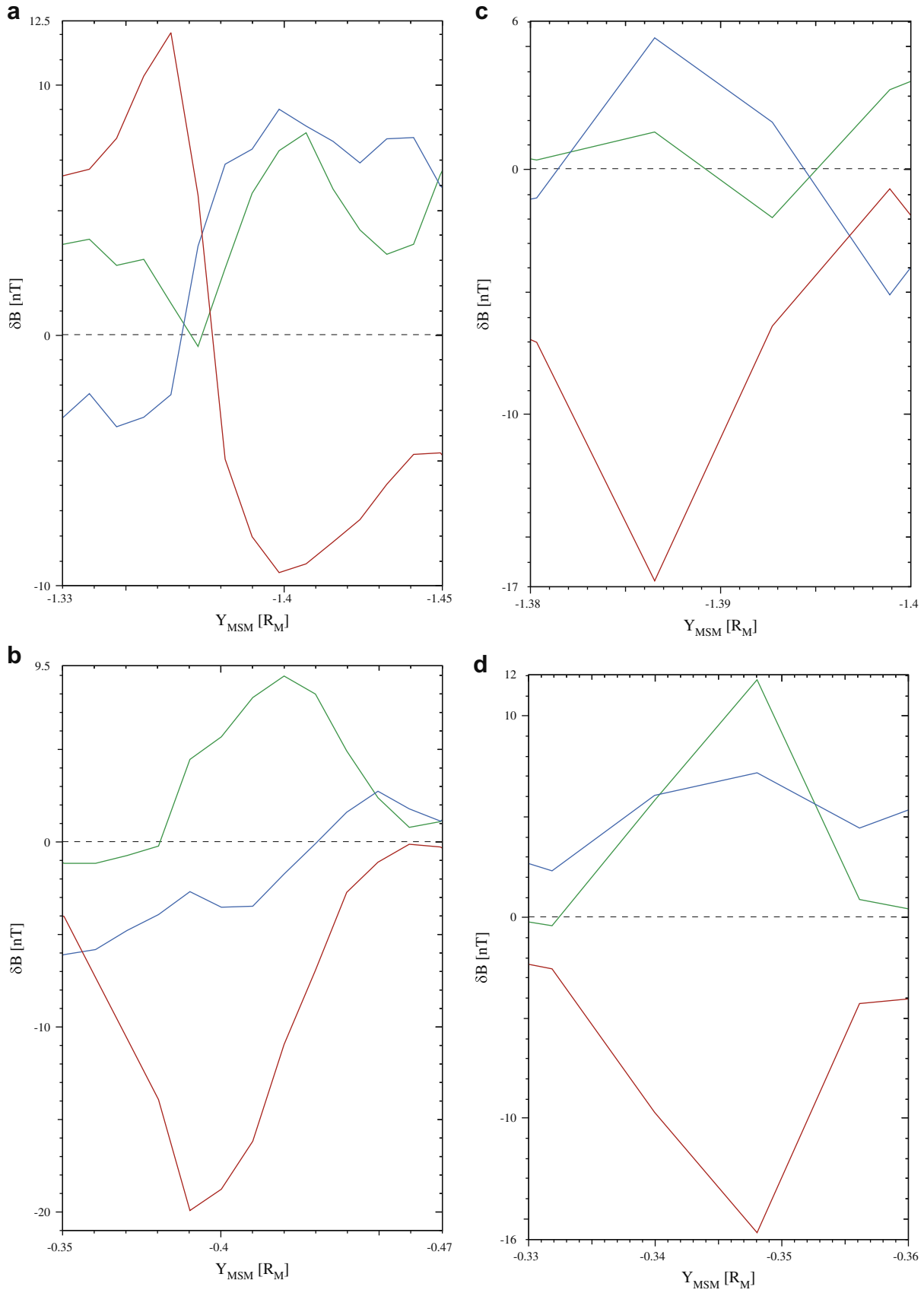

Fig. 10. Four examples of severe magnetic field excursions not incorporated in the best-fitting model of this paper. (a and c) Two examples from M1. (b and d) Two examples from M2.

Please cite this article in press as: Alexeev, I.I., et al. Mercury's magnetospheric magnetic field after the first two MESSENGER flybys. Icarus (2010), doi:10.1016/j.icarus.2010.01.024

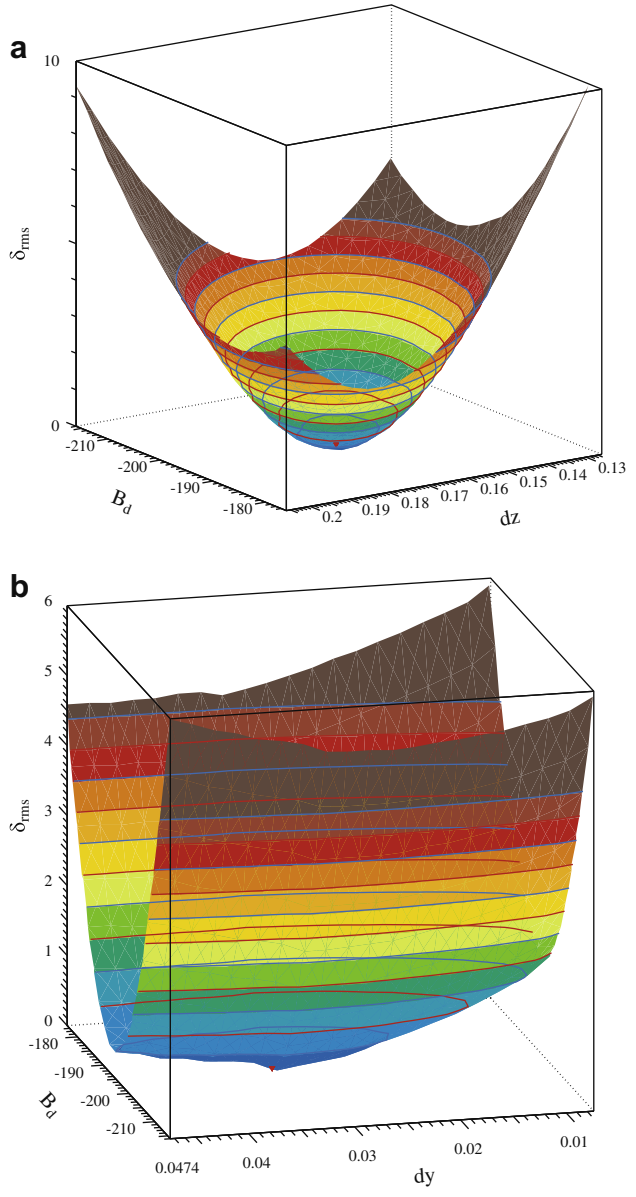

Fig. 11. The dependence of the difference $\delta_{\rm rms}$ = rms − rms$_{min}$ on dipole parameters. (a) Dependence on dipole equatorial field strength B_d and the dipole vertical offset dz. (b) Dependence on dipole equatorial field strength B_d and the dipole horizontal offset dy.

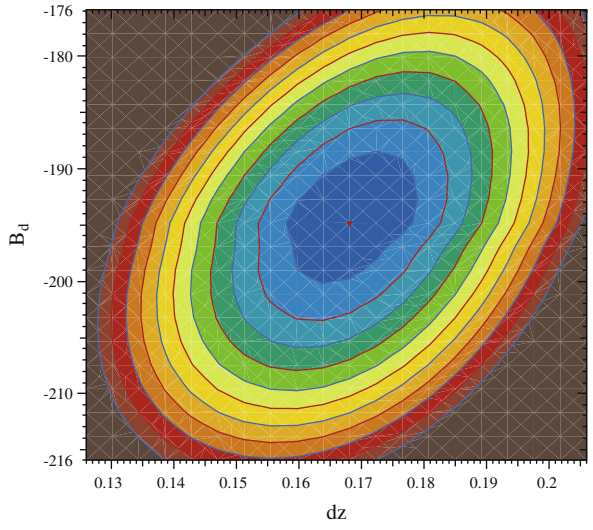

Fig. 12. Contours of $\delta_{\rm rms}$ = rms − rms$_{min}$ as a function of the dipole equatorial field strength B_d (vertical axis) and the dipole vertical offset dz (horizontal axis). The red dot shows the rms$_{min}$ position.

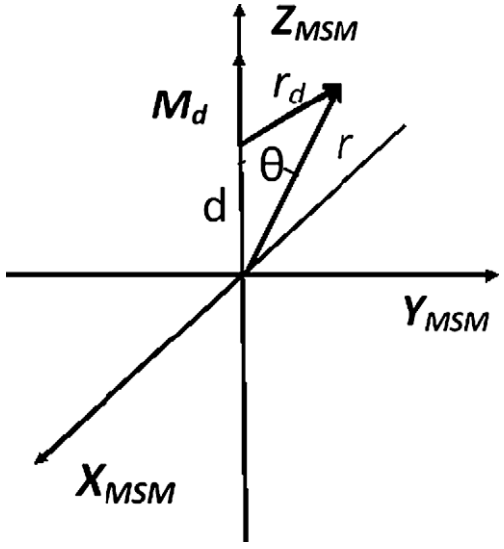

Fig. 13. The northward shift of Mercury's magnetic dipole.

After taking the derivative with respect to s we have:

$$\frac{\cos\theta - s}{(1 + s^2 - 2s\cos\theta)^{3/2}} = \sum_{n=1}^{\infty} n s^{n-1} P_n(\cos\theta). \tag{11}$$

Eq. (11) gives the spherical harmonic expansion of the dipole potential for a shift along the Z-axis of a distance d. As is clear from Fig. 13, the distance to the dipole is $r_d = r\sqrt{1 + s^2 - 2s\cos\theta}$, where $s = d/r$ is a relative dipole displacement in the northward direction, r is the distance to the origin, and θ is the polar angle. The distance along the Z-axis to the point (r, θ) is $z_d = z - d = r(\cos\theta - s)$. Finally we have:

$$U_d = M_d \frac{z_d}{r_d^3} = M_d \frac{r\cos\theta - d}{r_d^3} = \frac{M_d}{r^2} \frac{\cos\theta - s}{(1+s^2-2s\cos\theta)^{3/2}},$$
$$\frac{M_d}{r^2} \frac{\cos\theta - s}{(1+s^2-2s\cos\theta)^{3/2}} = \frac{M_d}{r^2} \sum_{n=1}^{\infty} n s^{n-1} P_n(\cos\theta). \tag{12}$$

Here $M_d = -196\ \text{nT} \cdot R_M^3$ is the dipole magnetic moment. From Eq. (12) one can calculate the Gauss coefficients for the shifted dipole:

$$g_1^0 = -196\ \text{nT}, \quad g_2^0 = 2g_1^0 d/R_M = -65\ \text{nT}, \quad \text{and}$$
$$g_3^0 = 3g_1^0 d^2/R_M^2 = -16.2\ \text{nT}. \tag{13}$$

Anderson et al. (2010) give −213 nT and −66 nT for the dipole and quadrupole terms with an rms misfit of 14 nT. To calculate the spherical harmonic coefficients of the external (magnetospheric) sources we use the formula:

$$V(r,\theta,\varphi) = \sum_{n=1}^{\infty}\sum_{m=0}^{n}(g_n^m \cos m\varphi + h_n^m \sin m\varphi)\left(\frac{R_M}{r}\right)^{n+1} P_n^m(\cos\theta)$$
$$+ \sum_{n=1}^{\infty}\sum_{m=0}^{n}(G_n^m \cos m(\varphi - \lambda_{Sun})$$
$$+ H_n^m \sin m(\varphi - \lambda_{Sun}))\left(\frac{r}{R_M}\right)^{n} P_n^m(\cos\theta), \tag{14}$$

where λ_{Sun} is the eastern longitude of the noon meridian (or subsolar point). We have used three different noon longitudes for the four encounters: $\lambda_{Sun\_M10} = 260^\circ$ for M10 I and M10 III, $\lambda_{Sun\_M1} = 185^\circ$ for

M1, and $\lambda_{Sun\_M2} = 3^\circ$ for M2. Because Uno et al. (2009), in their spherical harmonic expansions of the external field, ignored longitudinal differences in the Sun–Mercury line for the different flybys we cannot compare directly the external coefficients of Uno et al. (2009) with our results. For the main axially symmetric external term G_1^0, the phase λ_{Sun} does not matter and we can compare it with the value of Anderson et al. (2010). For our model the corresponding coefficient can be calculated as $G_1^0 = \frac{2}{3}\frac{M_d}{R_1^3} = 47.6$ nT for an average subsolar distance $R_1 = 1.4\ R_M$. Anderson et al. (2010) give $G_1^0 = 47$ nT, which is in good agreement with our model.

The results in this paper of fitting observations from the Mariner 10 and MESSENGER flybys with the paraboloid magnetosphere model demonstrate that during each flyby Mercury's magnetosphere has displayed different states. Those states correspond to different subsolar distances, different distances to the inner edge of the tail currents, different tail lobe fluxes and polar cap sizes, different vertical displacements of the tail current-sheet plane, and different amounts of IMF penetration.

The subsolar magnetopause magnetic field strength that balances solar wind dynamic pressure is given in Table 4. From the magnetic balance equation at the subsolar magnetopause, we calculated the solar wind dynamic pressure, p_{dyn}, for each flyby. Also given in Table 4 is the subsolar magnetopause field, $B_{m,}$ which has been calculated with the approximation (Alexeev et al., 2006):

$$B_m(R_1) = B_{dip} + B_{CF} = 2.44 \cdot B_{dip} = 2.44\frac{M_d}{R_1^3}, \qquad (15)$$

where $B_{dip} = M_d/R_1^3$ is the dipole field at the subsolar magnetopause, and B_{CF} is the Chapman-Ferraro field at the same point, $B_{CF} = 1.44\ B_{dip}$ for the paraboloid magnetopause. The subsolar magnetopause magnetic field strength B_m was calculated from the best-fit model parameters for each encounter. The solar wind density n_{sw} was calculated from p_{dyn} under four assumed values of solar wind velocity (Table 4). For M10 I and III the solar wind velocity was previously V_{sw} estimated by Slavin and Holzer (1979b), and for M1 and M2 the velocity was chosen to be constant and equal to 400 km/s. As can be expected from the subsolar magnetopause distance, R_1, the most severe solar wind was during the inbound pass of the M10 I encounter. Quieter ("average") solar wind conditions were encountered during the outbound M10 I pass and during M1. For these periods the solar wind pressure is estimated to be 1.5 times smaller than during the inbound pass of M10 I. During M10 III the solar wind dynamic pressure was 2.6 times weaker than during M10 I.

The derived solar wind stand-off distance for M1, $R_1 = 1.35\ R_M$, is in good agreement with the previous result $R_1 = 1.4\ R_M$ obtained by Slavin et al. (2009a). MESSENGER cannot observe the solar wind, but solar magnetograph-driven models of the solar wind were used to predict a ram pressure, p_{sw}, of ~16 nPa for M1 (Baker et al., 2009), a value close to that calculated here. These estimates of p_{sw} and R_1 may be used to compute the magnetic moment of Mercury from the pressure balance condition for a dipolar magnetosphere (Slavin et al., 2009a). The result is $B_{d0} = 212$ nT (Slavin et al., 2009a), where B_{d0} is the equatorial field of Mercury, a value consistent with our estimate.

The opposite orientation of the north–south component of the interplanetary magnetic field during M1 and M2 observations is a unique feature of these data as it allows study of reconnection effects in Mercury's magnetosphere. Following Mercury orbit insertion (MOI) in March 2011, MESSENGER will execute two passes through the magnetosphere per Earth day. The anticipated wealth of data will allow the influence of the IMF on Mercury's magnetosphere to be studied in much more detail. Also, the planetary dipole moment will be defined more accurately. Finally, the data from the orbital phase will allow for a much-improved assessment of the tail current sheet.

Table 4
Subsolar magnetopause magnetic field.

Flyby	2.44 B_{dip}	B_m, nT	p_{dyn}, nPa	n_{sw}, cm^{-3}	V_{sw}, km/s
M10 1 in	229.9	239.5	22.8	22.7	550
M10 1 out	191.9	198.2	15.6	15.6	550
M10 III	163.3	180.6	13.0	10.9	600
M1	193.6	196.0	15.3	28.8	400
M2	175.2	167.5	11.1	21.0	400
Average	190.6	196.4	15.6	19.5	500

10. Summary

Our results may be summarized as follows:

1. Our estimation of Mercury's dipole field gives the smallest rms deviation yet between model predictions and Mariner 10 and MESSENGER data, 10.7 nT, comparing favorably to the rms misfit of 14–19 nT given by Anderson et al. (2010) and 24 nT by Uno et al. (2009). The derived dipole moment for Mercury is 196 nT. R_M^3. The dipole is offset from Mercury's center by 405 km in the northward direction. The dipole inclination to Mercury's rotation axis is relatively small, ~4°, with a longitude of 193°E for the north pole.
2. This level of agreement between model and data is possible only because the magnetospheric current system parameters have been determined separately for each flyby. The magnetospheric stand-off distance, the distance from the planet's center to the inner edge of the tail current sheet, the tail lobe magnetic flux, and the displacement of the tail current sheet relative to the Mercury solar-magnetospheric equatorial plane have been determined independently for each flyby.
3. Our model is based on the *a priori* assumption that the dipole position and the moment orientation and strength do not change in time. The Mercury solar-magnetospheric coordinates are determined by the dipole parameters (the dipole moment orientation and dipole offset). As a result, the contribution of magnetospheric currents to the total magnetospheric field depends on the dipole parameters. The good agreement has been obtained by an interactive procedure at each step of which the dipole was determined simultaneously for all flybys, following which the specific magnetospheric state was determined separately for each flyby. The final fit was reached after several tens of steps.
4. Mercury rotates about its spin axis relatively slowly, and the effect of its rotation can be ignored during the short duration of each flyby (about 30 min). But in our fitting procedure, we had to take into account the different positions of the Sun in Mercury's sky for each specific flyby. The time intervals between Mariner 10 and MESSENGER flybys were 34–35 years, and the interval between the first two MESSENGER flybys was nine months, both longer than one Mercury sidereal day. Thus, the Sun's longitude in the Mercury body-fixed coordinate system differed markedly among the flybys.
5. We analyzed the contributions of two magnetospheric current systems to the magnetic field measured along the MESSENGER flyby trajectories: (a) the magnetopause and (b) the tail currents. The maximum of the B_z component of the dipole term is +125 nT, the maximum of the tail current contribution to the B_z component of the magnetospheric field is about two times smaller in amplitude at −50 nT, and the magnetopause current adds +32 nT at the boundary between dawn flank of

Please cite this article in press as: Alexeev, I.I., et al. Mercury's magnetospheric magnetic field after the first two MESSENGER flybys. Icarus (2010), doi:10.1016/j.icarus.2010.01.024

the magnetosphere and magnetosheath, nearly compensating for the tail current contribution at this region. For the inbound M1 and M2 passes, both of which were close to the tail current sheet, the dipole term is less than 30% of the total magnetic field. The relative contributions from the various sources are different for the individual components of the magnetic field vector. The B_y component is controlled primarily by the dipole terms, but the dipole contributions to the B_x component on the inbound part of the MESSENGER trajectory are negligible. In this region the tail current contribution was dominant for M2.

6. We speculate that when MESSENGER entered the magnetosphere during M1 the spacecraft passed inside the plasma sheet, whereas during M2 MESSENGER passed south of the tail current and measured only the southern lobe magnetic field. The magnetic field variations at the M1 inbound magnetopause crossing indicate that the spacecraft entered through the dusk flank of the tail into the central plasma sheet (Slavin et al., 2008). The significant tailward tilting of this magnetic field even close to the planet is due to the presence of a strong cross-tail current sheet.
7. To minimize the deviation between model and observations for each flyby, three constant components of the vector $\boldsymbol{B}_i$ were added to the model field. This term can be considered as magnetic field of some current systems that are not included in our model, such as field-aligned currents or induction currents. For M1 this term is about 15 nT, and for M2 it is less than 4 nT.
8. We have no simultaneous measurements of plasma and magnetic field inside the magnetosphere and in the neighboring solar wind. However, from our study we may conclude that the influence of the IMF on the magnetospheric magnetic field structure is strong. The differences in the current systems between the first and second MESSENGER flybys are attributed to the effects of strong magnetic reconnection driven by southward IMF during the latter flyby.

Acknowledgments

Work at the Institute of Nuclear Physics, Moscow State University, was supported by the RFBR Grants 07-05-00529 and 09-02-92603-KO_a. I.I.A. thanks Igor Sitnik for his practical advice on the FUMILI method and for his teaching how to run the FUMILIM code. The MESSENGER project is supported by the NASA Discovery Program under contracts NASW-00002 to the Carnegie Institution of Washington and NAS5-97271 to the Johns Hopkins University Applied Physics Laboratory.

Appendix A. Model description

Here we repeat a short description of the Mercury paraboloid magnetospheric model (Alexeev et al., 2008). The name of this model is derived from its key simplifying assumption that the magnetopause can be represented as a paraboloid of revolution along the planet-Sun line. The fields due to the magnetopause currents and tail current system are obtained using a method pioneered by Alexeev (1978) wherein the magnetic fields of the various magnetospheric sources are confined inside the magnetopause by adding appropriate shielding fields. Paraboloid models have also been developed and successfully tested against magnetic field measurements taken at Jupiter and Saturn (Belenkaya, 2004, 2009; Belenkaya et al., 2005, 2006, 2007; Alexeev and Belenkaya, 2005; Alexeev et al., 2006). As mentioned earlier, this model is robust in that the amount of open magnetic flux in the polar cap and the effects of the interplanetary magnetic field intensity and direction can be specified in a manner appropriate to each planetary magnetosphere.

The model uses Mercury's dipole-centered solar-magnetospheric coordinate (MSM) system described in Section 4, whereby Mercury's magnetic moment $\boldsymbol{M}_d$ lies in the X–Z plane of the MSM coordinate system. The main contributors to the magnetic field in Mercury's miniature magnetosphere considered in our model are: (i) the intrinsic magnetic (dipole) field of the planet and the magnetopause current that confines the dipole field inside the magnetopause, (ii) the dawn-to-dusk-directed cross-tail currents and their closure currents on the magnetopause, and (iii) the IMF that partially penetrates into the magnetosphere as a result of "reconnection" with the planetary magnetic field.

The following parameters define Mercury's magnetospheric magnetic field in the paraboloid model: (i) the distance R_1 from Mercury's center to the subsolar point on the magnetopause; (ii) the distance R_2 from the planet's center to the inner edge of the magnetospheric tail current sheet; (iii) the magnetic field B_{d0} at the surface equator due to the dipole field only; (iv) the magnitude of the magnetic field at the inner edge of the tail current sheet due to the current sheet alone, B_t/α_0, where $\alpha_0 = (1 + 2R_2/R_1)^{1/2}$; (v) the tilt angle ψ between the magnetic dipole direction and the Z_{MSM} direction; (vi) the displacement z_0 of the tail current sheet relative to the magnetic equatorial plane $z_{MSM} = 0$; and (vii) the portion, $\boldsymbol{b}$, of the IMF, $\boldsymbol{B}$, penetrating into magnetosphere, given as

$$\boldsymbol{b} = k_r \boldsymbol{B}, \tag{A1}$$

where k_r is the reconnection efficiency coefficient which determines the IMF penetration into the magnetosphere. Tsyganenko (2002) found the best correspondence between his model of Earth's inner magnetosphere and observations of IMF penetration into the magnetosphere for k_r values between 0.15 and 0.8. For comparison, Slavin and Holzer (1979a) estimated the efficiency of the dayside reconnection at Mercury to be 40% due to the low solar wind Alfvén Mach numbers typical of the inner heliosphere.

The magnetopause is approximated as a paraboloid of revolution

$$2xR_1 = 2R_1^2 - y^2 - z^2. \tag{A2}$$

The appropriateness of such a shape for the forward magnetopause is supported by the boundary fitting of Russell (1977) and Slavin et al. (2009b). Russell (1977), for example, found a near-paraboloid shape, i.e., eccentricity 0.8 versus 1.0 for a true parabola, for Mercury's magnetopause from Mariner 10 observations. With these assumptions the paraboloid model formulation of Alexeev (1986) can be used to calculate the magnetic configuration of Mercury's magnetosphere.

A.1. Screened dipole magnetic field

An initial solution of the problem of the screened planetary dipole field confined within a model magnetopause approximated by a paraboloid of revolution was obtained by Alexeev and Shabansky (1972). These authors presented a solution of the Laplace equation with a given potential derivative at the boundary (Neumann problem) by direct integration of the dipole magnetic field normal to magnetopause. Later Stern (1985) repeated this solution, but added a representation of the magnetopause current fields as a sum of Bessel harmonics. The next step was taken by Greene and Miller (1994), who conceived a simpler way to construct a solution and provided integral representations of the screened planetary dipole field within a paraboloid magnetopause with an arbitrary magnetopause flaring angle. This solution created the possibility of describing the magnetopause with an arbitrary ratio of the dawn–dusk magnetopause cross-section radius to the subsolar

magnetopause distance. Below we follow the Greene and Miller (1994) solution.

A detailed description of the screened planetary dipole field within the model magnetopause has been presented, for example, by Belenkaya et al. (2005) for the Jovian magnetosphere. The same method can be used to construct the topology of Mercury's magnetosphere. The coordinate transformation between parabolic coordinates (α, β, φ) and Mercury solar-magnetospheric Cartesian coordinates (x, y, z) is defined as follows:

$$x = \frac{R_1}{2}(\beta^2 - \alpha^2 + 1), \quad \alpha^2 = \frac{1}{2} + \frac{R_p - x}{R_1}, \tag{A3a}$$

$$y = R_1 \alpha\beta \sin\varphi, \quad \beta^2 = -\frac{1}{2} + \frac{R_p + x}{R_1}, \tag{A3b}$$

$$z = R_1 \alpha\beta \cos\varphi, \quad \tan\varphi = \frac{y}{z}, \tag{A3c}$$

where X points from the center dipole toward the Sun and the X–Z plane contains the planetary dipole, φ is the azimuthal angle about the X-axis, $R_p^2 = (x - R_1/2)^2 + y^2 + z^2$ is the square of the distance to the paraboloid focus, and R_1 is a scale length determining magnetopause size. The surfaces α = constant and β = constant form paraboloids of revolution about the X-axis of opposite curvature [for details, see Belenkaya et al. (2005)]. The magnetic field vector is transformed from parabolic into solar-magnetospheric Cartesian coordinates (x, y, z) using the relations:

$$B_x = -\frac{\alpha}{\sqrt{\alpha^2+\beta^2}} B_\alpha + \frac{\beta}{\sqrt{\alpha^2+\beta^2}} B_\beta,$$

$$B_y = \frac{\beta \sin\varphi}{\sqrt{\alpha^2+\beta^2}} B_\alpha + \frac{\alpha \sin\varphi}{\sqrt{\alpha^2+\beta^2}} B_\beta + \cos\varphi B_\varphi,$$

$$B_z = \frac{\beta \cos\varphi}{\sqrt{\alpha^2+\beta^2}} B_\alpha + \frac{\alpha \cos\varphi}{\sqrt{\alpha^2+\beta^2}} B_\beta - \sin\varphi B_\varphi.$$

Since the combined field (dipole plus magnetopause current field) is curl-free within the magnetosphere, it can be described by a scalar potential U ($\boldsymbol{B} = -\nabla U$):

$$U_{d+sd} = (U_d^{\parallel} + U_{sd}^{\parallel}) \sin\psi + (U_d^{\perp} + U_{sd}^{\perp}) \cos\psi, \tag{A4}$$

where $U_d^{\parallel}$ and $U_d^{\perp}$ are the scalar potentials that describe the dipole components parallel and perpendicular to the Mercury–Sun line, respectively, $U_{sd}^{\parallel}$ and $U_{sd}^{\perp}$ are the corresponding scalar potentials of the screening fields produced by the magnetopause currents, and ψ is the tilt angle of the dipole with respect to the Z_{MSM}-axis. In MSM Cartesian coordinates the dipole scalar potentials are

$$U_d^{\parallel} = \mu_M \frac{x}{r^3} \quad \text{and} \quad U_d^{\perp} = \mu_M \frac{z}{r^3}, \tag{A5}$$

where $4\pi\mu_M/\mu_o$ is Mercury's dipole moment ($\mu_M = 196\ \text{nT} \cdot R_M^3$), which was determined in Section 8 by fitting the flyby observations, and the dipole centric distance, r, is $r = \sqrt{x^2+y^2+z^2} = \frac{R_1}{2}\sqrt{(\alpha^2+\beta^2+1)^2 - 4\alpha^2}$.

The screened dipole magnetic field is then calculated using parabolic coordinates (Eq. (A2)) and the following integral transforms (e.g., Gradshteyn and Ryzhik, 1971)

$$\int_0^\infty \lambda^2 J_0(\lambda\alpha) K_0(\lambda\beta) J_1(\lambda) d\lambda = \frac{2(\beta^2 - \alpha^2 + 1)}{[(\alpha^2+\beta^2+1)^2 - 4\alpha^2]^{3/2}} = \frac{xR_1^2}{2r^3} = \frac{U_d^{\parallel}}{M_M}, \tag{A6a}$$

and

$$\int_0^\infty \lambda^2 J_1(\lambda\alpha) K_1(\lambda\beta) J_1(\lambda) d\lambda = \frac{4\alpha\beta}{[(\alpha^2+\beta^2+1)^2 - 4\alpha^2]^{3/2}} = \frac{zR_1^2}{2r^3\cos\varphi} = \frac{U_d^{\perp}}{M_M \cos\varphi}, \tag{A6b}$$

where the J_n are Bessel functions of the first kind, the K_n are modified Bessel functions that have a singularity at the origin, and the constant M_M is determined from the dipole moment and subsolar magnetopause distance as $M_M = 2\mu_M/R_1^3$. The formulas (A6) represent an expansion of the dipole potential on eigenfunctions of the Laplace operator (Bessel functions) in parabolic coordinates. We use here the Bessel-function definitions from Abramowitz and Stegun (1972). For an arbitrary function $f(\lambda)$, the integral $\int_0^\infty \lambda(\lambda\alpha)K_0(\lambda\beta)f(\lambda)d\lambda$ and the integral $\int_0^\infty \lambda J_1(\lambda\alpha)K_1(\lambda\beta)f(\lambda)d\lambda$ multiplied by $\cos\phi$ are the solutions to the Laplace equation in parabolic coordinates.

Using the transforms (A6) we can write the summed potential U_{d+sd} (Eq. (A4)) as

$$U_d^{\parallel} + U_{sd}^{\parallel} = M_M \int_0^\infty \lambda^2 J_1(\lambda) J_0(\lambda\alpha) \left(K_0(\lambda\beta) + I_0(\lambda\beta) \frac{K_1(\lambda)}{I_1(\lambda)} \right) d\lambda, \tag{A7a}$$

$$U_d^{\perp} + U_{sd}^{\perp} = M_M \cos\varphi \int_0^\infty \lambda^2 J_1(\lambda) J_1(\lambda\alpha) \left(K_1(\lambda\beta) - I_1(\lambda\beta) \frac{K_1'(\lambda)}{I_1'(\lambda)} \right) d\lambda, \tag{A7b}$$

where the primes indicate derivatives with respect to the argument, and the functions I_n are the modified Bessel functions that have no singularity inside the magnetosphere. After calculation of the derivative of β with respect to the function inside the brackets, and taking $\beta = 1$ (magnetopause), we can see that first and second terms inside the brackets cancel each other: $K_0'(\beta) = -I_1(\lambda)\frac{K_1(\lambda)}{I_1(\lambda)}$ and $K_1'(\lambda) = I_1'(\lambda)\frac{K_1'(\lambda)}{I_1'(\lambda)}$. The potential for the combined field, determined from Eqs. (A4) and (A7), confines the magnetic field inside the magnetosphere, i.e., $B_\beta = 0$ at the magnetopause. This can be verified from the following expressions for the magnetic field components in parabolic coordinates

$$B_\alpha = -\frac{1}{R_1\sqrt{\alpha^2+\beta^2}} \frac{\partial U}{\partial \alpha}, \tag{A8a}$$

$$B_\beta = -\frac{1}{R_1\sqrt{\alpha^2+\beta^2}} \frac{\partial U}{\partial \beta} \tag{A8b}$$

and,

$$B_\varphi = -\frac{1}{R_1\alpha\beta} \frac{\partial U}{\partial \varphi}. \tag{A8c}$$

A.2. Field of the tail current system

The model for the tail field adopted here is a modification of that previously proposed for the terrestrial (Alexeev et al., 2003) and jovian (Belenkaya et al., 2005) magnetospheres. The tail field can be presented as a sum of two contributions $\boldsymbol{B} = \boldsymbol{B}_1 + \boldsymbol{B}_2$. $\boldsymbol{B}_2$ provides the dominant contribution and is associated with the current flow in the tail current sheet, $\boldsymbol{j} = \text{curl}\, \boldsymbol{B}_2/\mu_o$. The tail current is closed via the tail magnetopause, and the component $\boldsymbol{B}_1$ describes the curl-free field within the magnetosphere associated with the current closure.

In parabolic coordinates we define $\boldsymbol{B}_2 = (B_{2\alpha}, 0, 0)$, where [see Belenkaya et al. (2005), for details]

$$B_{2\alpha} = B_t \begin{cases} 0 & \text{for } \alpha < \alpha_o, \\ \frac{f(\beta,\varphi)}{\alpha\sqrt{\alpha^2+\beta^2}} & \text{for } \alpha > \alpha_o. \end{cases} \tag{A9}$$

The field $B_{2\alpha}$ is divergence-free everywhere except on the surface $\alpha = \alpha_o$, where for $\alpha < \alpha_o$ the field and current both vanish. On the X-axis, the inner edge of the tail current sheet lies at a down-tail distance from the planet center given by $R_2 = R_1(\alpha_o^2 - 1)/2$, from which the constant $\alpha_o = \sqrt{1 + 2R_2/R_1}$ is determined. The divergence of $\boldsymbol{B}_2$ on $\alpha = \alpha_o$ is then accommodated by the curl-free field $\boldsymbol{B}_1$ as described below.

Please cite this article in press as: Alexeev, I.I., et al. Mercury's magnetospheric magnetic field after the first two MESSENGER flybys. Icarus (2010), doi:10.1016/j.icarus.2010.01.024

Table 5
Zeros, λ_{nk}, of the derivative of the Bessel functions, $J'_n(\lambda_{nk}) = 0$.

n/k	1	2	3	4	5
1	1.841183900	5.3314427000	8.5363163000	11.706005000	14.863588700
3	4.2011889412	8.0152365984	11.345924311	14.585848286	17.788747866
5	6.4156163752	10.519860874	13.987188630	17.312842488	20.575514521
7	8.5778364889	12.932386237	16.529365884	19.941853366	23.268052926
9	10.711433969	15.286737667	19.004593538	22.501398726	25.891277276
11	12.826491226	17.600266557	21.430854238	25.008518704	28.460857279

The function $f(\beta, \phi)$ in Eq. (A9) determines the current profile within the current sheet, for which we choose $f(\beta, \varphi) = sign\left(\frac{\pi}{2} - |\varphi|\right)$. Our choice of the function $f(\beta, \phi)$ corresponds to the infinitely thin current sheet because the function $f(\beta, \phi)$ effectively depends only on φ. The function $f(\beta, \phi)$ can be written also as

$$f(\beta, \varphi) = \sum_{n=1}^{\infty} \sum_{k=1}^{\infty} f_{nk} J_n(\lambda_{nk}\beta) \cos n\varphi, \tag{A10}$$

where λ_{nk} is a solution of the equation $J'_n(\lambda_{nk}) = 0$, as required for zero normal field at the magnetopause, and we require only those terms with $n = 2m + 1$ odd in our application by the anti-symmetry of the field about the equatorial plane. The first six zeros λ_{nk} for $n = 1, 3, \ldots, 11$ are given in Table 5. Using the first five terms of the expansion (A10) yields an accuracy of about one part in 10^5 (see Belenkaya et al., 2005).

The coefficients f_{nk} in Eq. (A10) can be calculated by taking into account the properties of the orthogonal functions as

$$f_{nk} = \frac{4}{\pi} \frac{(-1)^m}{n} C_{nk} \quad \text{where } C_{nk} = N_{nk}^{-1} \int_0^1 J_n(\lambda_{nk}\beta)\beta\, d\beta, \tag{A11}$$

and the normalizing coefficient N_{nk} is given by $N_{nk} = \frac{1}{2}\left(1 - \frac{n^2}{\lambda_{nk}^2}\right) J_n^2(\lambda_{nk})$. The numerical coefficients C_{nk} used in this paper were calculated by numerical integration of Eq. (A11) and are shown in Table 6. We have taken the terms in the sums in Eqs. (A13) and (A14) from $n = 1$ to 11 (n odd only), and from $k = 1$ to 6. To check the accuracy of this truncation, the ratio $B_\beta/|B|$ at the magnetopause has been calculated and is smaller than 10^{-3} everywhere (see also Belenkaya et al., 2005).

The total magnetic flux in each lobe of the distant tail is a constant for $\alpha \to \infty$ since there is no normal component at the magnetopause and $B_z \to 0$ on the tail center plane. This value is $F_\infty = 0.5\pi B_t R_1^2$. This equation can be used to determine B_t in Eq. (A8):

$$B_t = \frac{2F_\infty}{\pi R_1^2}, \tag{A12}$$

if the tail magnetic flux, F_∞, the subsolar distance, R_1, and the inner edge current distance, R_2, are specified.

Combining $\boldsymbol{B}_1$ and $\boldsymbol{B}_2$ to find the total tail field [see Belenkaya et al. (2005), for details], we finally have for $\alpha < \alpha_o$

$$B_\alpha = -\frac{B_t}{\sqrt{\alpha^2 + \beta^2}} \sum_{n=1}^{\infty} \sum_{k=1}^{\infty} f_{nk}\lambda_{nk} K_n(\lambda_{nk}\alpha_o) J_n(\lambda_{nk}\beta) I'_n(\lambda_{nk}) \cos n\varphi, \tag{A13a}$$

$$B_\beta = -\frac{B_t}{\sqrt{\alpha^2 + \beta^2}} \sum_{n=1}^{\infty} \sum_{k=1}^{\infty} f_{nk}\lambda_{nk} K_n(\lambda_{nk}\alpha_o) J'_n(\lambda_{nk}\beta) I_n(\lambda_{nk}) \cos n\varphi, \tag{A13b}$$

and

$$B_\varphi = \frac{B_t}{\alpha\beta} \sum_{n=1}^{\infty} \sum_{k=1}^{\infty} f_{nk} n K_n(\lambda_{nk}\alpha_o) J_n(\lambda_{nk}\beta) I_n(\lambda_{nk}) \sin n\varphi, \tag{A13c}$$

while for $\alpha > \alpha_o$ we have

Table 6
Coefficients C_{nk} describing the tail magnetic field.

k/m	1	2	3	4	5	6
1	1.9799	2.9054	3.5014	3.9584	4.3359	4.6609
2	0.6216	1.3208	1.7698	2.1096	2.3870	2.6238
3	0.3699	0.8543	1.1898	1.4514	1.6683	1.8549
4	0.2710	0.6658	0.9565	1.1892	1.3848	1.5544
5	0.2118	0.5362	0.7842	0.9869	1.1594	1.3101

$$B_\alpha = -\frac{B_t}{\sqrt{\alpha^2 + \beta^2}} \left(\frac{f(\beta, \varphi)}{\alpha} + \sum_{n=1}^{\infty} \sum_{k=1}^{\infty} f_{nk}\lambda_{nk} I_n(\lambda_{nk}\alpha_o) J_n(\lambda_{nk}\beta) K'_n(\lambda_{nk}) \cos n\varphi \right), \tag{A14a}$$

$$B_\beta = -\frac{B_t}{\sqrt{\alpha^2 + \beta^2}} \sum_{n=1}^{\infty} \sum_{k=1}^{\infty} f_{nk}\lambda_{nk} I_n(\lambda_{nk}\alpha_o) J'_n(\lambda_{nk}\beta) K_n(\lambda_{nk}) \cos n\varphi, \tag{A14b}$$

and

$$B_\varphi = \frac{B_t}{\alpha\beta} \sum_{n=1}^{\infty} \sum_{k=1}^{\infty} f_{nk} n I_n(\lambda_{nk}\alpha_o) J_n(\lambda_{nk}\beta) K_n(\lambda_{nk}) \sin n\varphi. \tag{A14c}$$

Formulas (A13) and (A14) determine the tail-current magnetic field everywhere inside the Mercury magnetosphere. These formulas have been derived from continuity of all three components of the magnetic field vector on the surface $\alpha = \alpha_o$. We used the expansion of $sign\left(\frac{\pi}{2} - |\varphi|\right)$ on Fourier harmonic components, $sign\left(\frac{\pi}{2} - |\varphi|\right) = \frac{4}{\pi} \sum_{k=1}^{\infty} \frac{(-1)^{k+1}}{2k-1} \cos(2k-1)\varphi$, and the equality $I'_n(x)K_n(x) - I_n(x)K'_n(x) = 1/x$ to demonstrate that the tail-field component B_α is continuous at $\alpha = \alpha_o$ (see point 9.6.15 in Abramowitz and Stegun (1972)).

References

Abramowitz, M., Stegun, I.A., 1972. Handbook of Mathematical Functions, eighth ed. Dover, Mineola, NY, p. 177.
Alexeev, I.I., 1978. Regular magnetic field in the Earth's magnetosphere. Gemagn. Aeron. 18, 656–665 (in Russian, English transl. in Geomagn. Aeron. 18, 447–452).
Alexeev, I.I., 1986. The penetration of interplanetary magnetic and electric fields into the magnetosphere. J. Geomagn. Geoelectr. 38, 1199–1221.
Alexeev, I.I., Belenkaya, E.S., 2005. Modelling of the Jovian magnetosphere. Ann. Geophys. 23, 809–826.
Alexeev, I.I., Shabansky, V.P., 1972. A model of a magnetic field in the geomagnetosphere. Planet. Space Sci. 20, 117–133.
Alexeev, I.I., Belenkaya, E.S., Bobrovnikov, S.Yu., Kalegaev, V.V., 2003. Modelling of the electromagnetic field in the interplanetary space and in the Earth's magnetosphere. Space Sci. Rev. 107, 7–26.
Alexeev, I.I., Kalegaev, V.V., Belenkaya, E.S., Bobrovnikov, S.Yu., Bunce, E.J., Cowley, S.W.H., Nichols, J.D., 2006. A global magnetic model of Saturn's magnetosphere, and a comparison with Cassini SOI data. Geophys. Res. Lett. 33, L08101. doi:10.1029/2006GL025896.
Alexeev, I.I., Belenkaya, E.S., Bobrovnikov, S.Yu., Slavin, J.A., Sarantos, M., 2008. Paraboloid model of Mercury's magnetosphere. J. Geophys. Res. 113, A12210. doi:10.1029/2008JA013368.
Anderson, B.J., Acuña, M.H., Lohr, D.A., Scheifele, J., Raval, A., Korth, H., Slavin, J.A., 2007. The Magnetometer instrument on MESSENGER. Space Sci. Rev. 131, 417–450.
Anderson, B.J., Acuña, M.H., Korth, H., Purucker, M.E., Johnson, C.L., Slavin, J.A., Solomon, S.C., McNutt Jr., R.L., 2008. The structure of Mercury's magnetic field from MESSENGER's first flyby. Science 321, 82–86.
Anderson, B.J., and 11 colleagues, 2010. The magnetic field of Mercury. Space Sci. Rev., in press.

Please cite this article in press as: Alexeev, I.I., et al. Mercury's magnetospheric magnetic field after the first two MESSENGER flybys. Icarus (2010), doi:10.1016/j.icarus.2010.01.024

Baker, D.N., and 11 colleagues, 2009. Space environment of Mercury at the time of the first MESSENGER flyby: Solar wind and interplanetary magnetic field modeling of upstream conditions. J. Geophys. Res. 114, A10101. doi:10.1029/2009JA014287.

Belenkaya, E.S., 2004. The Jovian magnetospheric magnetic and electric fields: Effects of the interplanetary magnetic field. Planet. Space Sci. 52, 499–511.

Belenkaya, E.S., 2009. Magnetospheres of magnetized planets. Phys. Usp. 179, 809–835 (in Russian, English transl. in Phys. Usp. 52 (8), 809–835).

Belenkaya, E.S., Bobrovnikov, S.Yu., Alexeev, I.I., Kalegaev, V.V., Cowley, S.W.H., 2005. A model of Jupiter's magnetospheric magnetic field with variable magnetopause flaring. Planet. Space Sci. 53, 863–872.

Belenkaya, E.S., Cowley, S.W.H., Alexeev, I.I., 2006. Saturn's aurora in the January 2004 events. Ann. Geophys. 24, 1649–1663.

Belenkaya, E.S., Alexeev, I.I., Blokhina, M.S., Cowley, S.W.H., Badman, S.V., Kalegaev, V.V., Grigoryan, M.S., 2007. IMF dependence of the open-closed field line boundary in Saturn's ionosphere, and its relation to the UV auroral oval observed by the Hubble Space Telescope. Ann. Geophys. 25, 1215–1226.

Bergan, S., Engle, I.M., 1981. Mercury's magnetosphere and magnetotail revisited. J. Geophys. Res. 86, 2828–2836.

Boardsen, S.A., Anderson, B.J., Acuña, M.H., Slavin, J.A., Korth, H., Solomon, S.C., 2009. Narrow-band ultra-low-frequency wave observations by MESSENGER during its January 2008 flyby through Mercury's magnetosphere. Geophys. Res. Lett. 36, L01104. doi:10.1029/2008GL036034.

Christon, S.P., 1987. A comparison of the Mercury and Earth magnetospheres: Electron measurements and substorm time scales. Icarus 71, 448–471.

Connerney, J.E.P., Ness, N.F., 1988. Mercury's magnetic field and interior. In: Vilas, F., Chapman, C.R., Matthews, M.S. (Eds.), Mercury. University of Arizona Press, Tucson, pp. 494–513.

Dymov, S.N., Kurbatov, V.S., Silin, I.N., Yashenko, S.V., 2000. Constrained minimization in the C++ environment. Nucl. Inst. Methods Phys. Res. A 440, 431–437.

Engle, I.M., 1997. Mercury's magnetosphere: Another look. Planet. Space Sci. 45, 127–132.

Fraser-Smith, A.C., 1987. Centered and eccentric geomagnetic dipoles and their poles, 1600–1985. Rev. Geophys. 25, 1–16.

Gradshteyn, I.S., Ryzhik, I.M., 1971. Tables of Integrals, Sums, Expansions and Products. Nauka, Moscow, p. 689 (points 6.525 (1) (in Russian) (See also Tables of Integral Transforms, vol. II. McGraw-Hill Book Company, New York, NY, 1954, formula (8), p. 63)).

Greene, J.M., Miller, R.L., 1994. The field of a screened magnetic dipole. Planet. Space Sci. 42, 895–902.

Korth, H., Anderson, B.J., Acuña, M.H., Slavin, J.A., Tsyganenko, N.A., Solomon, S.C., McNutt Jr., R.L., 2004. Determination of the properties of Mercury's magnetic field by the MESSENGER mission. Planet. Space Sci. 52, 733–746.

Ness, N.F., Behannon, K.W., Lepping, R.P., Whang, Y.C., Schatten, K.H., 1974. Magnetic field observations of near Mercury: Preliminary results from Mariner 10. Science 185, 151–160.

Ness, N.F., Behannon, K.W., Lepping, R.P., Whang, Y.C., 1975. The magnetic field of Mercury. J. Geophys. Res. 80, 2708–2716.

Ness, N.F., Behannon, K.W., Lepping, R.P., Whang, Y.C., 1976. Observations of Mercury's magnetic field. Icarus 28, 479–488.

Ogilvie, K.W., Scudder, J.D., Vasyliunas, V.M., Hartle, R.E., Siscoe, G.L., 1977. Observations at the planet Mercury by the plasma electron instrument: Mariner 10. J. Geophys. Res. 82, 1807–1824.

Russell, C.T., 1977. On the relative locations of the bow shocks of the terrestrial planets. Geophys. Res. Lett. 4, 387–390.

Silin, I.N., 1976. Appendix III, Statisticheski metodi v eksperimentalnoi fizike, Atomizdat (translated into Russian from Eadie, W.T., Drijard, D., James, F.E., Roos, M., Sadoulet, B., 1971. Statistical Methods in Experimental Physics. North-Holland, Amsterdam).

Silin, I.N., 1983. FUMILI, CERN Program Library, D510.

Siscoe, G.L., Ness, N.F., Yeates, C.M., 1975. Substorms on Mercury. J. Geophys. Res. 80, 4359–4363.

Sitnik, I.M., 2008. Modification of the FUMILI minimization package (preprint JINR E11-2008-43, Dubna).

Slavin, J.A., Holzer, R.E., 1979a. On the determination of the Mercury magnetic moment: A critical review. Phys. Earth Planet. Int. 20, 231–236.

Slavin, J.A., Holzer, R.E., 1979b. The effect of erosion on the solar wind stand-off distance at Mercury. J. Geophys. Res. 84, 2076–2082.

Slavin, J.A., and 10 colleagues, 2007. MESSENGER: Exploring Mercury's magnetosphere. Space Sci. Rev. 131, 133–160.

Slavin, J.A.and 18 colleagues, 2008. Mercury's magnetosphere after MESSENGER's first flyby. Science 321, 85–89.

Slavin, J.A., and 17 colleagues, 2009a. MESSENGER observations of Mercury's magnetosphere during northward IMF. Geophys. Res. Lett. 36, L02101. doi:10.1029/2008GL036158.

Slavin, J.A., and 17 colleagues, 2009b. MESSENGER observations of magnetic reconnection in Mercury's magnetosphere. Science 324, 606–610.

Solomon, S.C., and 20 colleagues, 2001. The MESSENGER mission to Mercury: Scientific objectives and implementation. Planet. Space Sci. 49, 1445–1465.

Stern, D., 1985. Parabolic harmonics in magnetospheric modeling: The main dipole and the ring current. J. Geophys. Res. 90, 10851–10863.

Tsyganenko, N.A., 2002. A model of the near magnetosphere with a dawn–dusk asymmetry, 1. Mathematical structure. J. Geophys. Res. 107, 1179. doi:10.1029/2001JA000219.

Uno, H., Johnson, C.L., Anderson, B.J., Korth, H., Solomon, S.C., 2009. Modeling Mercury's internal magnetic field with smooth inversions. Earth Planet. Sci. Lett. 285, 328–339.

Please cite this article in press as: Alexeev, I.I., et al. Mercury's magnetospheric magnetic field after the first two MESSENGER flybys. Icarus (2010), doi:10.1016/j.icarus.2010.01.024